ERDC/CRREL TR-22-10

Cold Regions Research and Engineering Laboratory

US Army Corps of Engineers®
Engineer Research and Development Center

ERDC
ENGINEER RESEARCH & DEVELOPMENT CENTER

Thermal Infrared Comparison Study of Buried Objects between Humid and Desert Test Beds

M. Musty, V. Truong, J. L. Clausen, S. Frankenstein,
C. Williams, A. Trautz, S. Howington, and R. Kala

August 2022

The U.S. Army Engineer Research and Development Center (ERDC) solves the nation's toughest engineering and environmental challenges. ERDC develops innovative solutions in civil and military engineering, geospatial sciences, water resources, and environmental sciences for the Army, the Department of Defense, civilian agencies, and our nation's public good. Find out more at www.erdc.usace.army.mil.

To search for other technical reports published by ERDC, visit the ERDC online library at https://erdclibrary.on.worldcat.org/discovery.

ERDC/CRREL TR-22-10
August 2022

Thermal Infrared Comparison Study of Buried Objects between Humid and Desert Test Beds

M. Musty, V. Truong, J. L. Clausen, S. Frankenstein, C. Williams, A. Trautz, S. Howington, and R. Kala

U.S. Army Engineer Research and Development Center
Cold Regions Research and Engineering Laboratory
72 Lyme Road
Hanover, NH 03755-1290

Final report

Prepared for US Army Combat Capabilities Command

Under PE 0602712A/Project 468349/Task A1010, "Modernizing Environmental Signature Physics for Target Detection"

Abstract

This study pertains to the thermal variations caused by buried objects and their ramifications on soil phenomenology. A multitude of environmental conditions were investigated to observe the effect on thermal infrared sensor performance and detection capabilities. Correlations between these external variables and sensor contrast metrics enable determinable key factors responsible for sensor degradation. This document consists of two parts. The first part is a summary of data collected by the U.S. Army Corps of Engineers, Engineer and Research and Development Center Cold Regions Research and Engineering Laboratory (ERDC-CRREL), ERDC-Geotechnical Structures Laboratory, and Desert Research Institute at the Yuma Proving Ground (YPG) site in February 2020 and observations from this activity. The second part is a comparison of target visibility between data collected at YPG and data collected at the ERDC-CRREL test site in 2018.

Contents

Figures and Tables

Figures

Tables

Preface

This study was conducted for the U.S. Army Combat Capabilities Development Command (CCDC) C5ISR (Command, Control, Communications, Computers, Cyber, Intelligence, Surveillance, and Reconnaissance) Center formerly known as the US Army Communications-Electronics Research, Development and Engineering Center (CERDEC) Night Vision and Electronic Sensors Directorate (NVESD) under PE 0602712A/Project 468349/Task A1010, "Modernizing Environmental Signature Physics for Target Detection." The program monitor was Dr. Robert Davis.

The work was performed by the Engineer Research Development Center Cold Regions Research and Engineering Laboratory (ERDC-CRREL) Research and Engineering Division and the U.S. Army Engineer Research and Development Center Geotechnical Structures Laboratory (ERDC-GSL). At the time of publication, Mr. Nathan Lamie was Chief, Biochemical Sciences Branch; Dr. John Weatherly was Chief, Terrestrial and Cryospheric Sciences Branch; Dr. Melisa Nallar was Acting Chief, Engineering Resources Branch; and Dr. Caitlin A. Callaghan was Division Chief. Dr. Robert Davis was the Technical Director for Geospatial Research and Engineering/Military Engineering. The Acting Deputy Director of ERDC-CRREL was Mr. Bryan E. Baker, and the Director was Dr. Joseph L. Corriveau.

COL Christian Patterson was the Commander of ERDC, and Dr. David Pittman was the ERDC Director.

This report was revised 31 August 2022 for minor corrections. While it supersedes the previous version, the changes do not impact the reliability of the scholarly content.

Acronyms and Abbreviations

ASD	Analytical Spectral Devices
bgs	below ground surface
C5ISR	Command, Control, Communications, Computers, Cyber, Intelligence, Surveillance, and Reconnaissance
CBR	California Bearing Ratio
CCDC	U.S. Army Combat Capabilities Development Command
CERDEC	formerly known as the US Army Communications-Electronics Research, Development and Engineering Center
CRREL	Cold Regions Research and Engineering Laboratory
DRI	Desert Research Institute
ECOND	Electrical conductivity
EO	Electro-optical
ERDC	Engineer research And Development Center
FTIR	Fourier-transform Infrared Spectroscopy
GSL	Geotechnical and Structures Laboratory
Hz	hertz
IR	Infrared
LIDAR	Light detection and ranging
LWIR	Lone-wave infrared
md	metal deep
ms	metal shallow
MWIR	Mid-wave infrared
NVESD	Night Vision and Electronic Sensors Directorate
pd	plastic deep
ps	plastic shallow
Qf	Quaternary Fan
USACE	U.S. Army Corps of Engineers
VWC	Volumetric water content
XRF	X-ray Fluoroscopy
YPG	Yuma Proving Ground

Unit Conversion Factors

Multiply	By	To Obtain
degrees (angle)	0.01745329	radians
degrees Fahrenheit	(F-32)/1.8	degrees Celsius
degrees Fahrenheit	(F-32)/1.8+273.15	degrees Kelvin
feet	0.3048	meters
inches	2.54	centimeters
ounces (mass)	0.02834952	kilograms

1 Introduction

In an ongoing effort to study the impacts of environmental factors influencing thermal infrared (IR) sensors for the purposes of buried object detection (Clausen et al. 2020), a team of researchers from the U.S. Army Corps of Engineers (USACE) Engineer research and Development Center Cold Regions Research and Engineering Laboratory (ERDC-CRREL), ERDC-Geotechnical and Structures Laboratory (GSL), and Desert Research Institute (DRI) visited the Yuma Proving Ground (YPG) test site (Figure 1) in February 2020 to conduct in situ observations with a multitude of instruments. Targets from CRREL were transported to YPG, along with CRREL's thermal IR camera. This study additionally utilized a mid-wave IR and electro-optical (EO) camera to aid in investigating the target's changing contrast metrics with variable environmental conditions. The study began on February 10, 2020, at 13:30:00 and concluded on February 21, 2020, at 10:00:00. No precipitation was recorded during the study other than on Day 1, which resulted in 2.8 mm of afternoon rain.

1.1 Background

Thermal IR as a sensor modality is affected by a host of environmental conditions. Soil/material variability and porosity, soil disturbance, moisture migration/evaporation, and terrestrial radiant reflection and emittance can reduce the capability for object detection. Increases in moisture affect soil emissivity, which can especially hinder thermal imagery, where wet soil at low temperatures can appear like dry soils at higher temperatures (Hausner et al. 2020). This increase in soil moisture along with an increase in soil density also increases thermal conductivity, leading to drastic electromagnetic attenuation (Koh and Wakeley 2009). The dielectric properties between dry and wet soils can also vary up to an order of magnitude, with higher dielectric constants found in older and less porous soils such as those at YPG (Crews et al. 2019). Electromagnetic propagation in soil is quantified as the soil's bulk dielectric permittivity, which is affected by the soil's physical and chemical properties (Hausner et al. 2019). In addition, diurnal thermal fluctuations due to changing solar input throughout the day give rise to thermal contrasts at the soil surface (Khanafer and Vafai 2002; van De Griend et al. 1985) and, coupled with higher soil heterogeneity, lead to increases in thermal spatial variability. A

buried object only adds to this complexity by interfering with both heat and moisture transfer within the soil (Pan and Mahrt 1987).

Understanding the relationship between meteorological conditions and soil properties is paramount to detecting objects buried in soil and to predict sensor performance. An analytical solution requires extensive knowledge of the buried material, surface soil composition, soil water content, and humidity of the atmosphere. The quantification of these environmental effects will help in improving current detection algorithms through a process of strategic elimination (Howington et al. 2019).

1.2 Objective

Previous studies of how environmental conditions impact thermal sensor performance were finite, and this lack of environmental variability limited IR performance predictability. Qualitatively understanding how meteorological and soil phenomenology affect the temporal and spatial thermal variance of the terrain can aid in calibration and processing to detect buried objects, in addition to optimizing standoff performance and post-analysis. The magnitude of environmental variables monitored and the various biomes utilized in this work are, to the best of our knowledge, unprecedented. Developing a strong correlation between the environmental parameters and target detectability with the data sets collected at CRREL and YPG will allow for improved automatic target recognition (ATR) performance.

1.3 Approach

Targets like those installed at the CRREL test bed were deployed to YPG and buried at various depths in local soil. Electro-optical (EO) and IR sensors from mid to long-wave were utilized to track target visibility under varying environmental conditions over 11 days. A metric based on the disparity between target and background was collated with these external variables. Univariate and multivariate correlations were studied and analyzed for the purposes of dimensional reduction, in addition to validating our understanding of the phenomena responsible for soil temporal and spatial thermal variance.

2 Methods

2.1 General site information

The test site at YPG was located in lane 35 between objects 51 and 53, and spans 3 surface lithologic units, Qf1, Qf2 and Qf3 (Quaternary Fan, i.e., specific geologic period), as can be observed in Figure 1. The intrinsic and transient properties of the soil at YPG vary both between different lanes and within the same lane, consisting of four different soil types from different alluvial fan deposits (Hausner et al. 2019).

Figure 1. YPG Top View and Lane Map. Lower left legend denotes the quaternary fan. Lane 35 (red star) spans the surface lithologic unit Qf1, Qf2 and Qf3.

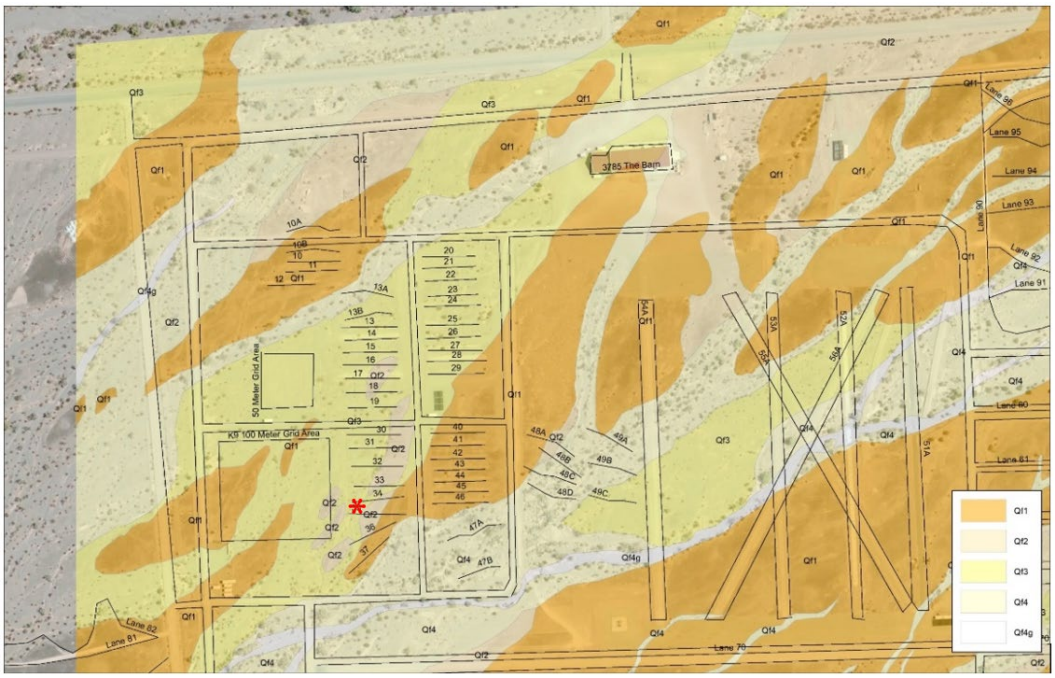

Already encamped in the lane is object 52 (a large type 72 plastic object filled with Composition B high explosives (Figure 2) and buried at 15.24 cm below ground surface (bgs) in 2014). Our addition includes four rectangular boxes (two plastic and two aluminum, each 40 × 40 × 20 cm) filled with fertilizer and local soil (Figure 3), which were placed in the corners of the plot as can be seen in Figure 4's dugout. One plastic and one aluminum box were each buried 5 cm bgs (shallow), and the remaining two boxes were buried 20 cm bgs (deep). Six 8 cm diameter pucks spray painted desert brown (three plastic and three aluminum) were also placed on the ground surface in the plot (Figure 5).

Figure 2. Target 52 located in Lane 35 at YPG.

Figure 3. Rectangular boxes buried in the YPG test plot.

Figure 4. Layout of the test plot with location of excavations for object burial.

Figure 5. Surface targets placed in the test lane.

2.2 Instrumentations

Four cameras were used to observe the test plot at a 5-minute resolution beginning February 13, 2020, at 12:15:00 and ending February 19, 2020, at 11:20:00 Mountain Standard Time (UTC-7). The four cameras used were

- Electro-optical (EO) camera with field of view 17 cm east of pin 52 and 48 cm west of pin 53
- FLIR A310F 90 long-wave infrared (LWIR)
- FLIR A6703 sc mid-wave infrared (MWIR)
- FLIR T640 (LWIR)

Figure 6. Cameras overlooking the test plot at YPG.

The cameras (Figure 6) are referred to in the remainder of the document with abbreviations EO, A310, MWIR, and LWIR, respectively. The EO is an EO Netcam XL 3MP camera with 0.8 cm lens with image resolution of 2048 × 1536 pixels and a maximum transfer speed of 225 frames/second. The EO camera has a Sony 1.27 cm charge-coupled device sensor with an exposure range of 1/100,000 to 1.3 seconds. The A310 is a FLIR A310F 90, an LWIR camera with a 90 x 73° field of view and 320 × 240 pixel resolution with a 30 hertz (Hz) frame rate. The MWIR (3.0–5.0 µm waveband) is an FLIR A6703 sc, an MWIR camera with an image acquisition speed of 480 frames/second and which produces 327,680 finely detailed pixel images. The MWIR has 640 × 512 resolution with a pixel size of 15 µm. The LWIR is a FLIR T640 camera with a 5 × 19° field

of view, 30 Hz frame rate, and a resolution of 640 × 480 pixels. Both the A310 and LWIR operate in the thermal band, with the former having a 7.3 to 13 μm spectral range while the latter has a 7.5 to 14 μm range. The LWIR has a larger temperature range and superior thermal sensitivity and accuracy but lacks the ruggedness of the A310.

For meteorological data collection, wind speed and direction cups were placed to the west of the ERDC-CRREL tripod (Figure 7). Incoming and outgoing short-wave solar radiation was collected along with air temperature and relative humidity. Meteorological data for the test site were obtained at five-minute intervals from a meteorological station located 1.2 meters from the edge of the observation lane and a second meteorological station located approximately 300 m away on the YPG station. Collections for surface characterizations included volumetric water content (VWC), soil density, strength (DCP), X-ray fluoroscopy (XRF), spectral reflectance, thermal conductivity, and surface topography with a light detection and ranging sensor (LiDAR). Surface and buried sensors were also utilized, which included 20 temperature sensors which were painted desert brown, two heat flux plates, and six Campbell Scientific CS655 soil moisture sensors, which measure soil temperature, volumetric water content, bulk electrical conductivity, and relative dielectric permittivity. Moisture sensors were buried from 5 to 40 cm bgs, while the heat flux plates were installed 5 cm bgs. Additional details about the sensors are documented in Clausen et al. (2021), and Clausen et al. (2020). All data was stored on a Campbell Scientific CR1000 datalogger.

2.3 Plot layout

The layout of the plot can be seen in Figure 8. The blue circles denote the surface objects, the green circles denote the YPG pins, the red circles denote heat flux plates, the triangles denote surface sensors, and the buried objects have their corresponding labels. The YPG lane is indicated with the black lines. Specifics on CS655 soil moisture probe locations can be found in Appendix A.1, and the temperature thermistor locations in Appendix A.2.

Figure 7. Metrological instrumentation installed at the YPG test plot.

Figure 8. Test plot layout in Lane 35 at YPG.

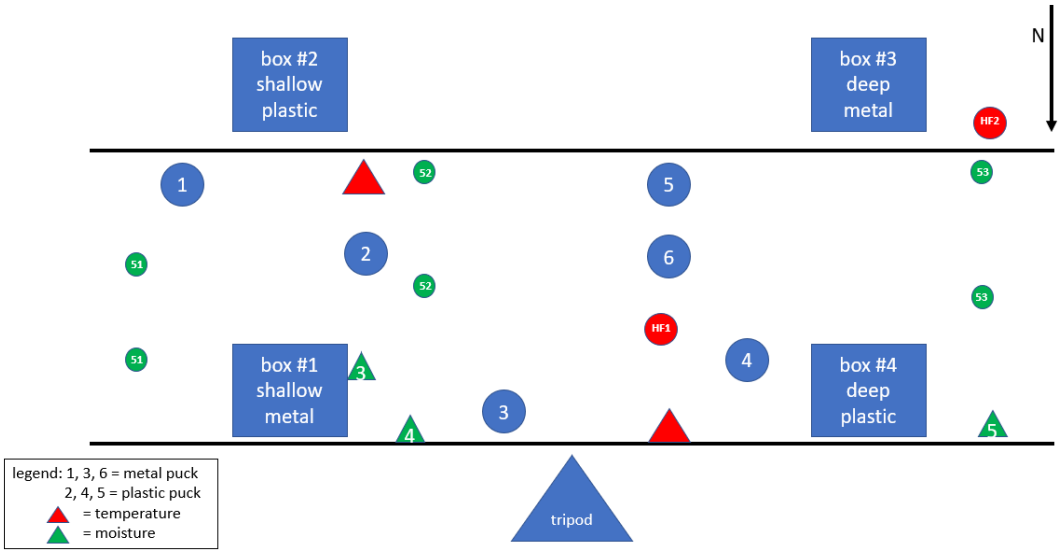

2.4 Measurements

On February 2, 2020, prior to target and sensor installment, DRI conducted terrain characterizations, measuring the soil's shear strength, density, Young's modulus, and California Bearing Ratio (CBR) with a 2.25 kg Clegg. On February 11, a LiDAR scan was conducted over the undisturbed surface, followed by erecting the ERDC-CRREL observation towers and metrological stations, and concluded with creating the dugout for the four CRREL targets. A Riegl VZ-400i was used to generate a

surface mesh over the full site with a 100 × 360° field of view and a maximum range of 400 m with 5 mm spatial accuracy.

On February 12, the targets were filled with lawn fertilizer mixed with native YPG soil (80:20) and buried in the test plot. Remaining instrumentations were installed, including GSL cameras, followed by further terrain characterization by GSL and DRI to measure the soil's spectral reflectance and thermal conductivity. Spectral data was collected with an analytical spectral devices (ASD) spectrometer and a Fourier-transform infrared spectroscopy (FTIR) spectrometer. The ASD is a FieldSpec 4 Hi-Res spectroradiometer with a measurement range of 350–2,500 nm, measurement accuracy of 0.5 nm, and a spectral resolution of 3 nm at 700 nm and 8 nm at 1400/2100 nm. The FTIR is a handheld Agilent 4300 and operates in the ranges of 2,222 to 15,385 nm with a spectral resolution of 4 to 16 cm^{-1}.

Thermal properties were measured with a KS-1 probe manufactured by Decagon Devices, Inc. (now Meter Group, Inc. USA) that houses a thermistor and a resistance heater capable of producing thermal conductivity and resistivity measurements with a range between 0.02 and 2.00 W/mK and 0.5 to 50 m/KW at an accuracy of ± 5% from 0.2 to 2 W/mK and ± 0.01 W/mK from 0.02 to 0.2 W/mK.

Finally, on February 13, XRF, soil density, and VWC were measured over the target boxes with Campbell Scientific CS655 probes. The CS655 sensors additionally measure temperature, bulk electrical conductivity, and relative dielectric permittivity, with an accuracy of ±3% VWC, ±0.05 dS/m, and ±0.5°C based on factory specifications. Measured field values are the average collected from five different locations every 2 hours. Note, the dielectric properties of the soil as measured by bulk electrical conductivity are used to infer the soil moisture content. Thus, the measured electrical conductivity is a function of the physical properties of the soil as well as the soil moisture content.

Since the probe is in a fixed location, the physical properties of the soil are unchanging and thus electrical conductivity is solely a function of changes in soil moisture. Campbell Scientific notes that soil moisture accuracy improves in soils with higher bulk electrical conductivity values. The soil density was measured with a Troxler EGauge Model 4590 surface density gauge. It measures the in-situ density and gravimetric water content at

5.1 cm intervals to a depth of 20.3 cm bgs to provide both the wet and dry soil densities with a repeatability and reproducibility of 1 standard deviation.

3 Data Analysis

The main objective of the data analysis is to identify environmental factors leading to an enhanced ability to identify and classify the various targets using the IR cameras and provide insight into the physical properties and forcing mechanisms behind the environmental conditions contributing to target visibility. Additionally, results from the data obtained at YPG and that from the collection of data in 2018 at the CRREL test plot (Clausen et al. 2021) are compared and contrasted, with the latter further divided into two groups (before and after target emplacement).

3.1 Environmental data summary

This study initiated with examining collected time series plots for the environmental data. Since the collection period at YPG was relatively short, we can visualize the entire duration of the study on a single plot, whereas CRREL data will be split with a focus on specific time periods. The variables for this study were chosen according to their potential applicability to operations in the field (i.e., easily obtainable and/or measured) and are summarized in Table 1.

Table 1. Environmental variable labels.

Description	CRREL Variable Label	YPG Variable Label
Incoming Solar Radiation	ShortWave_In_Avg	SR01Up_Avg
Reflected Solar Radiation	ShortWave_Reflect_Avg	SR01Dn_Avg
Air Temperature	AirTemp_Avg	AirTemp_Avg
Volumetric Water Content	vwc	vwc
Conductivity	econd	econd
Relative Humidity	Rh_Avg	Rh_Avg
Pressure	Pressure_Avg	Baro_Avg
Wind Speed	WndSpeed_Avg	WS_ms_Avg
Wind Direction	WndDir_Avg	WindDir_Avg

Radiometer data from YPG are shown in Figure 9, and a comparison of the radiometer data from YPG and CRREL (Clausen et al. 2021) is shown in Figure 10.

Figure 9. YPG radiometer data (W/m²) for the period February 13, 2020, at 1215 to February 19, 2020, at 1120 with (a) total incoming (UpTot), total reflected (DnTot), and net (UpTot-DnTot) radiation in W/m²; (b) incoming (SR01Up) and reflected (SR01Dn) shortwave radiation in W/m²; (c) incoming (IR01Up), reflected (IR01Dn), temperature corrected incoming and reflected (IR01UpCo and IR01DnCo) longwave radiation in W/m²; and (d) average albedo for the found surface.

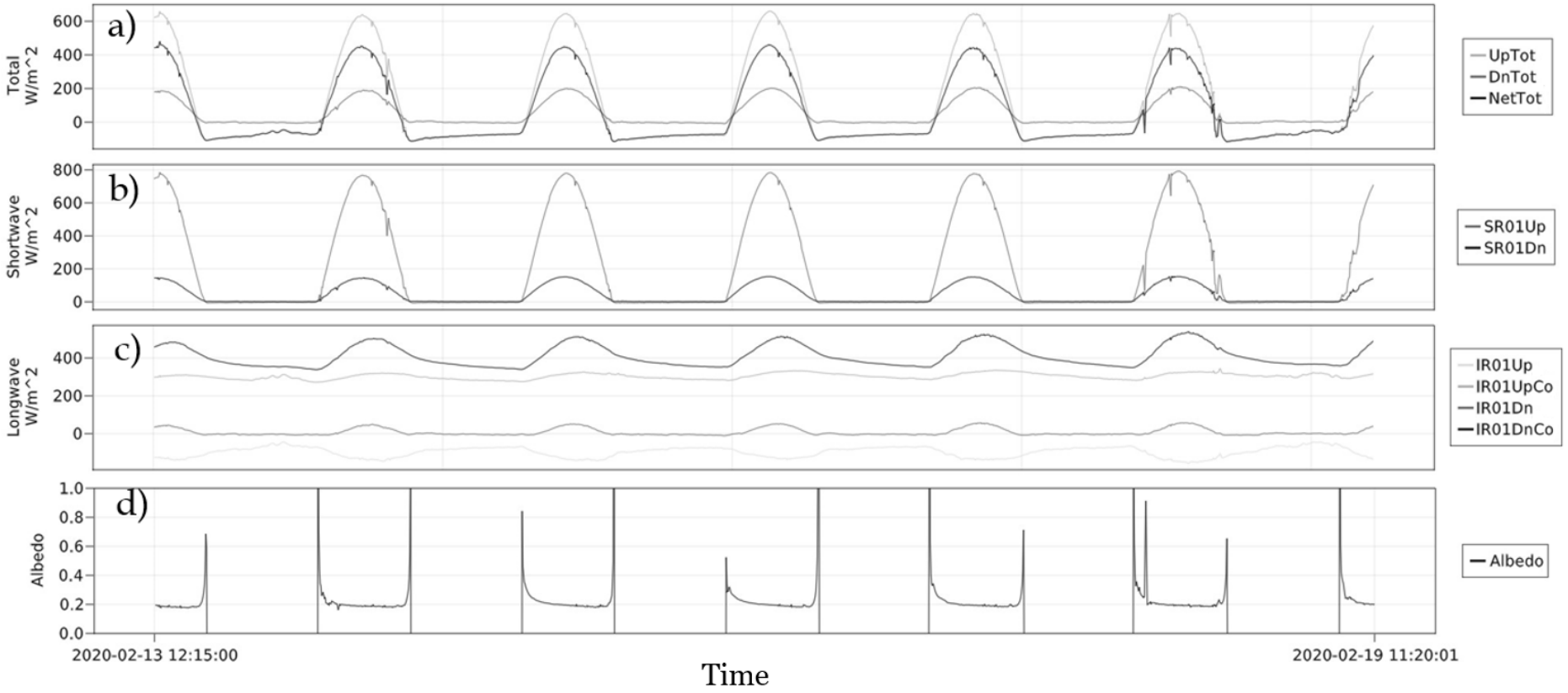

Figure 10. Yuma Proving Ground radiometer data compared to CRREL radiometer data, and depicts (a) incoming (SR01Up) and reflected (SR01Dn) shortwave radiation at YPG in W/m², (b) incoming (ShortWave_In) and reflected (ShortWave_Reflect) shortwave radiation at CRREL from late spring to midsummer 2018 in W/m², and (c) incoming (ShortWave_In) and reflected (ShortWave_Reflect) shortwave radiation at CRREL from midsummer to late autumn 2018 in W/m².

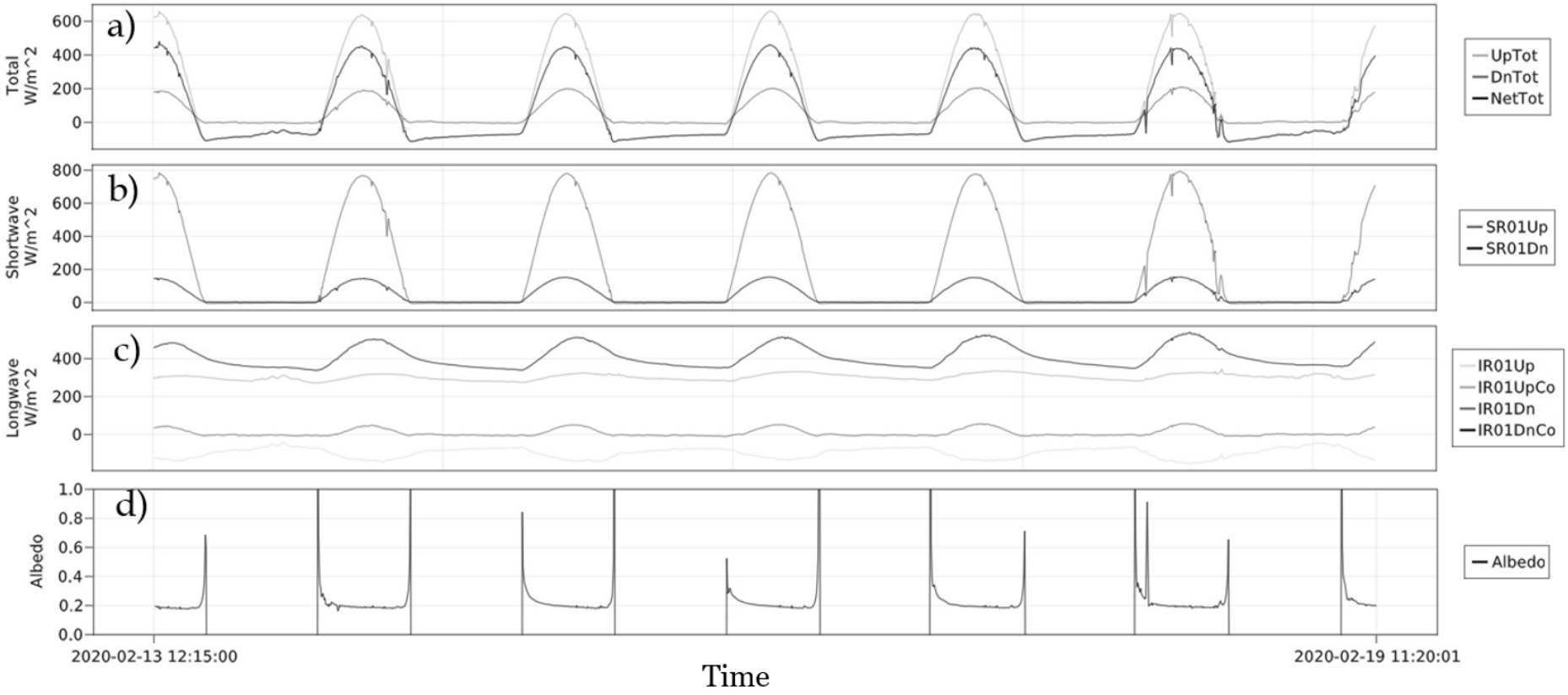

Because these two radiometers were different, only the short-wave radiation can be compared between the two studies. A notable feature from Figure 10 on the CRREL data is a seasonal trend of decreasing incoming solar radiation as winter approaches (Figure 10 *b*,*c*). In contrast, the YPG test was conducted in early February so despite a decrease in latitude, the sun angle and incoming solar radiation was lower. The duration of the test at YPG was too short to see the increase in incoming solar radiation as summer approaches. However, there is a period in September where the incoming solar radiation for the CRREL test was comparable to the YPG test with maximum values approximately 790 W/m^2. Both data sets also show a significant decrease in reflected shortwave radiation compared with the incoming, the reflected strength of which is dependent on the soil's dielectric constant (Davis and Annan 2002) and soil moisture (Mattikalli et al. 1998). Additionally, heat flux data from both studies are compared in Figure 11 and indicate slightly higher values for the YPG test than the CRREL test and are caused by a multitude of factors due to the variability in soil where physical, chemical, and transient properties affect electromagnetic propagation. This complexity leads to inconsistency and unpredictability (Hausner et al. 2019).

Figure 11. Heat flux [W/m²] data (FLX) from (a) YPG, (b) CRREL before target emplacement, and (c) CRREL after target emplacement.

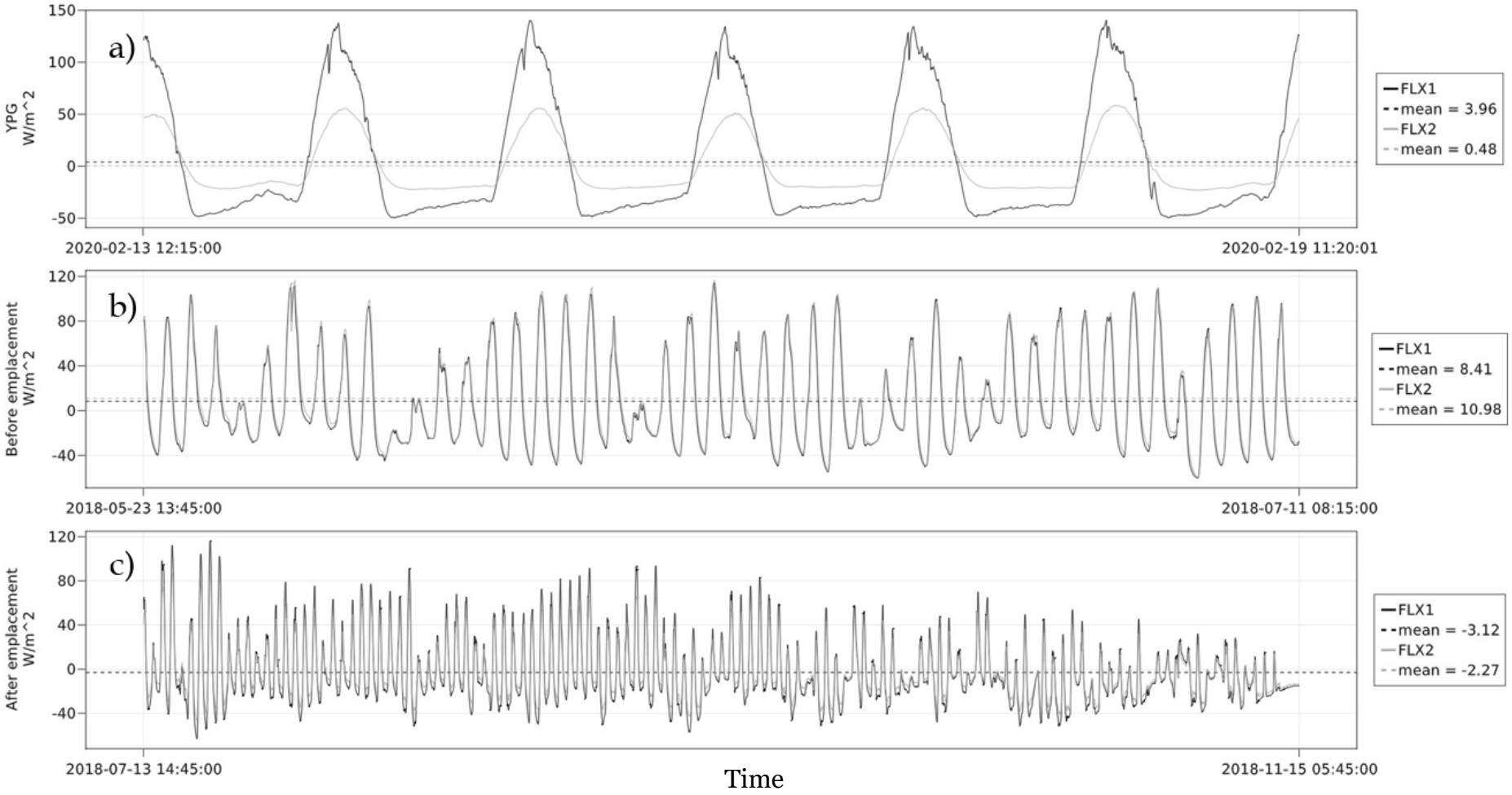

The heat flux data are extracted from two separate plates buried 5 cm bgs. Positive values indicate the soil is warming (receives energy), while negative values indicate the oppositive, *c* cooling (loosing energy). Buried objects obstruct the flow of water in the subsurface and thus the flow of energy transfer (Hausner et al. 2020). This phenomenon is evident in the last few peaks of Figure 11*b* when compared with the peaks of Figure 11.

Meteorological data (wind speed, wind direction, air temperature, pressure, and relative humidity) are shown in Figure 12 and Figure 13.

Soil temperature probe data are shown in Figure 14, and CS655 sensor data are shown in Figure 15, depicting the soil's VWC, electrical conductivity, and temperature.

Figure 12. YPG (a) wind speed (m/s) and (b) wind direction (degrees).

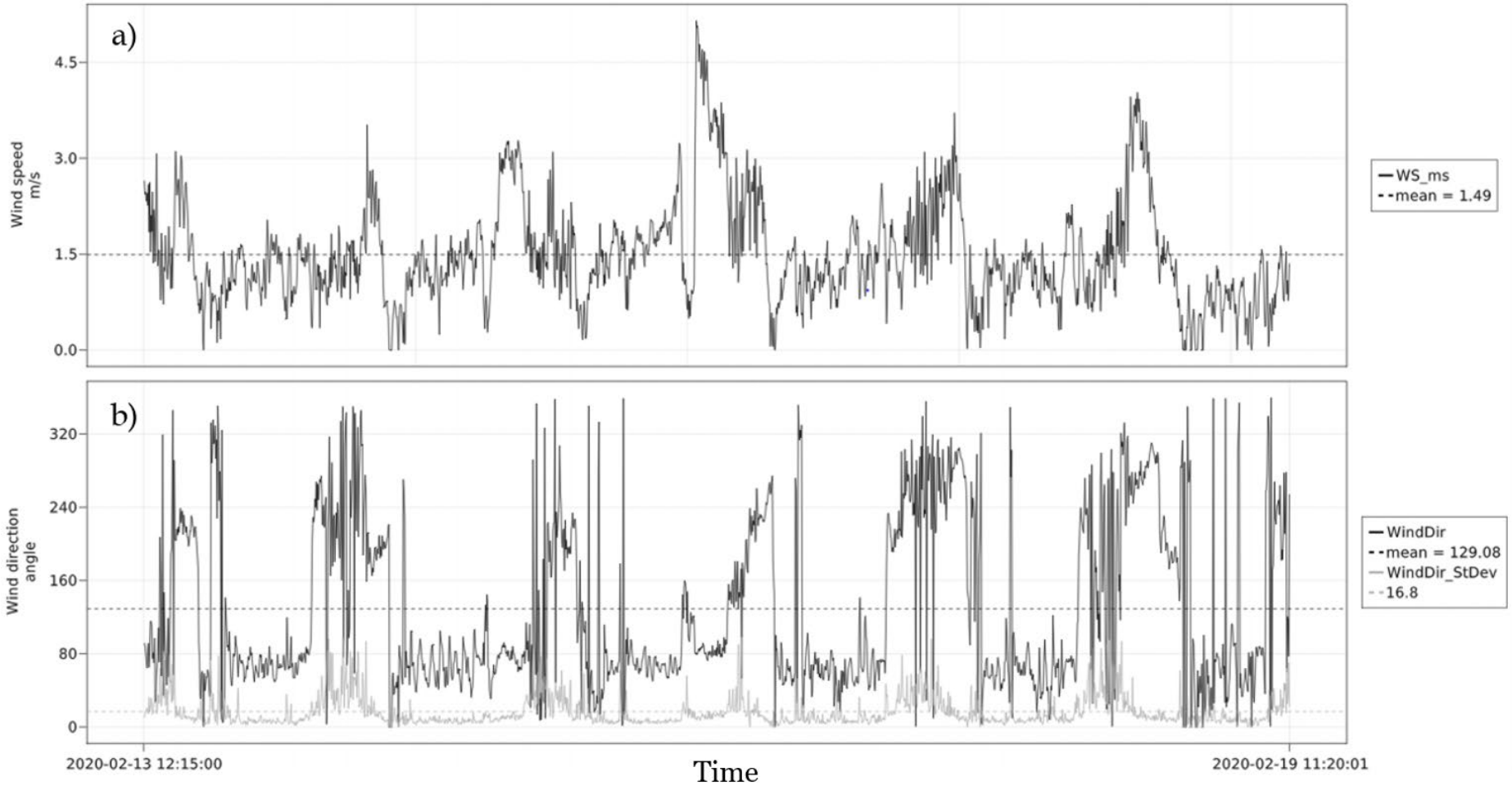

Figure 13. YPG (a) air temperature (°C), (b) pressure (mb), and (c) relative humidity (%).

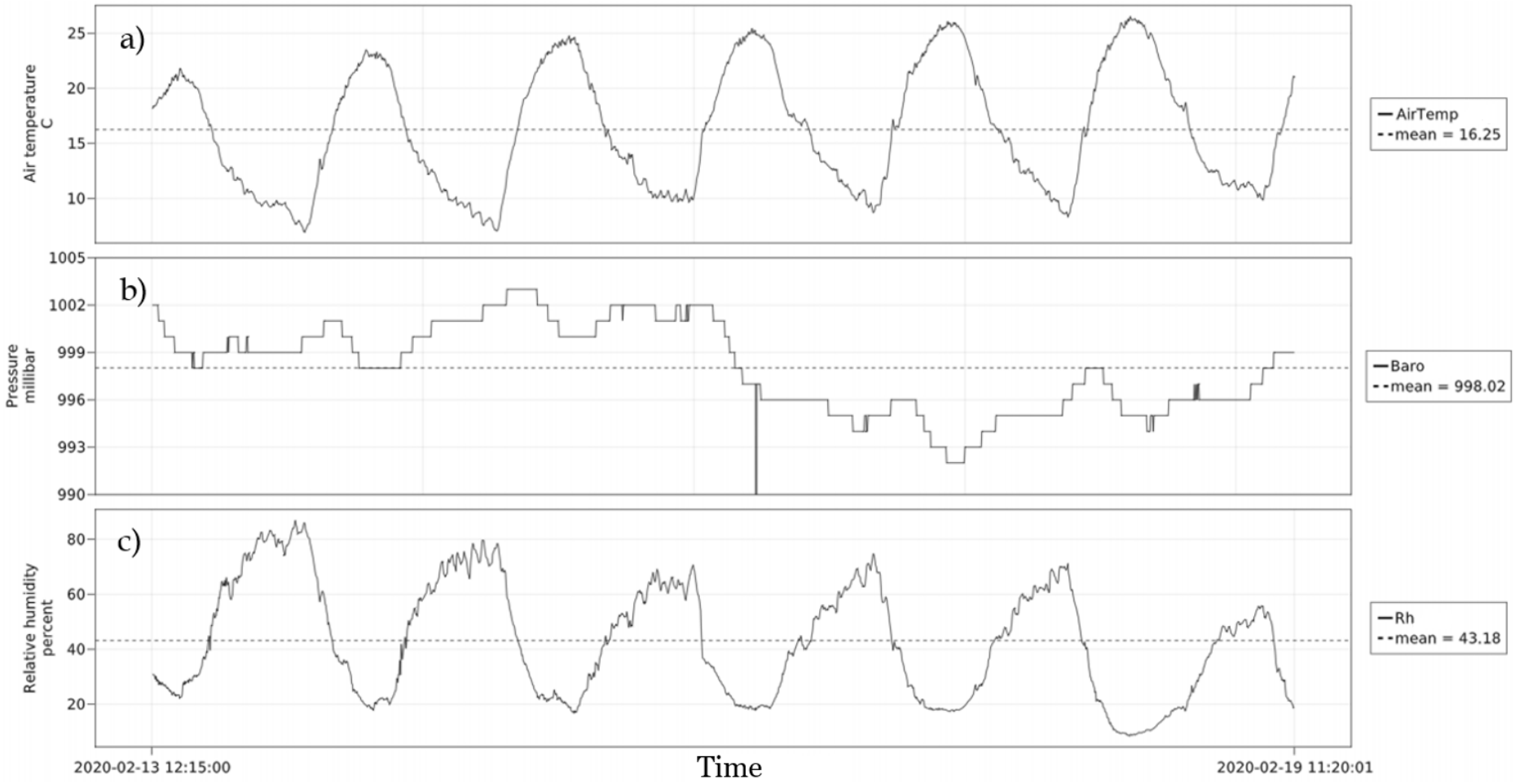

Figure 14. YPG soil temperature (°C) probe data.

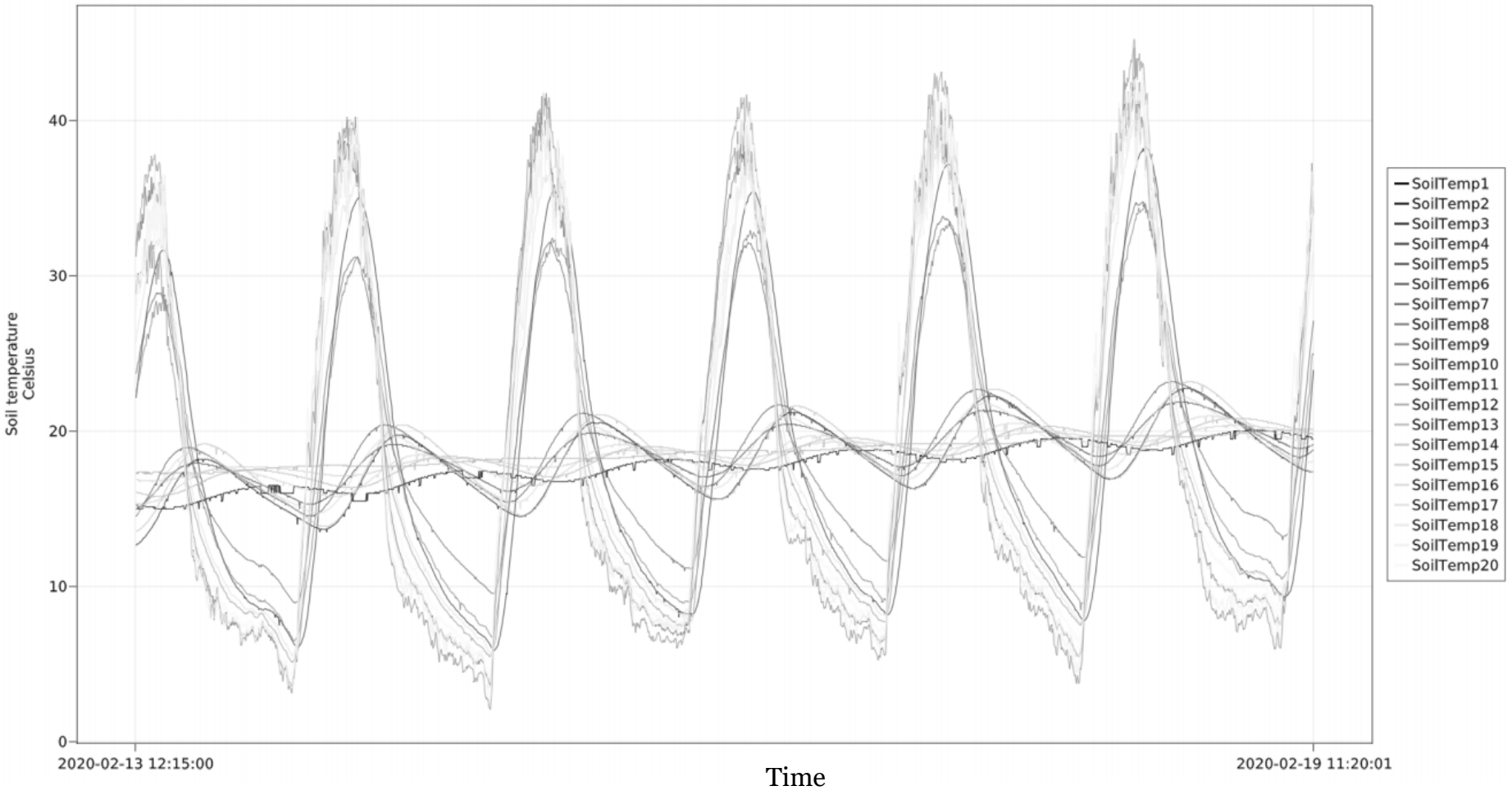

Figure 15. YPG CS655 data depicting (a) volumetric water content (%), (b) electrical conductivity (dS/m), and (c) temperature (°C).

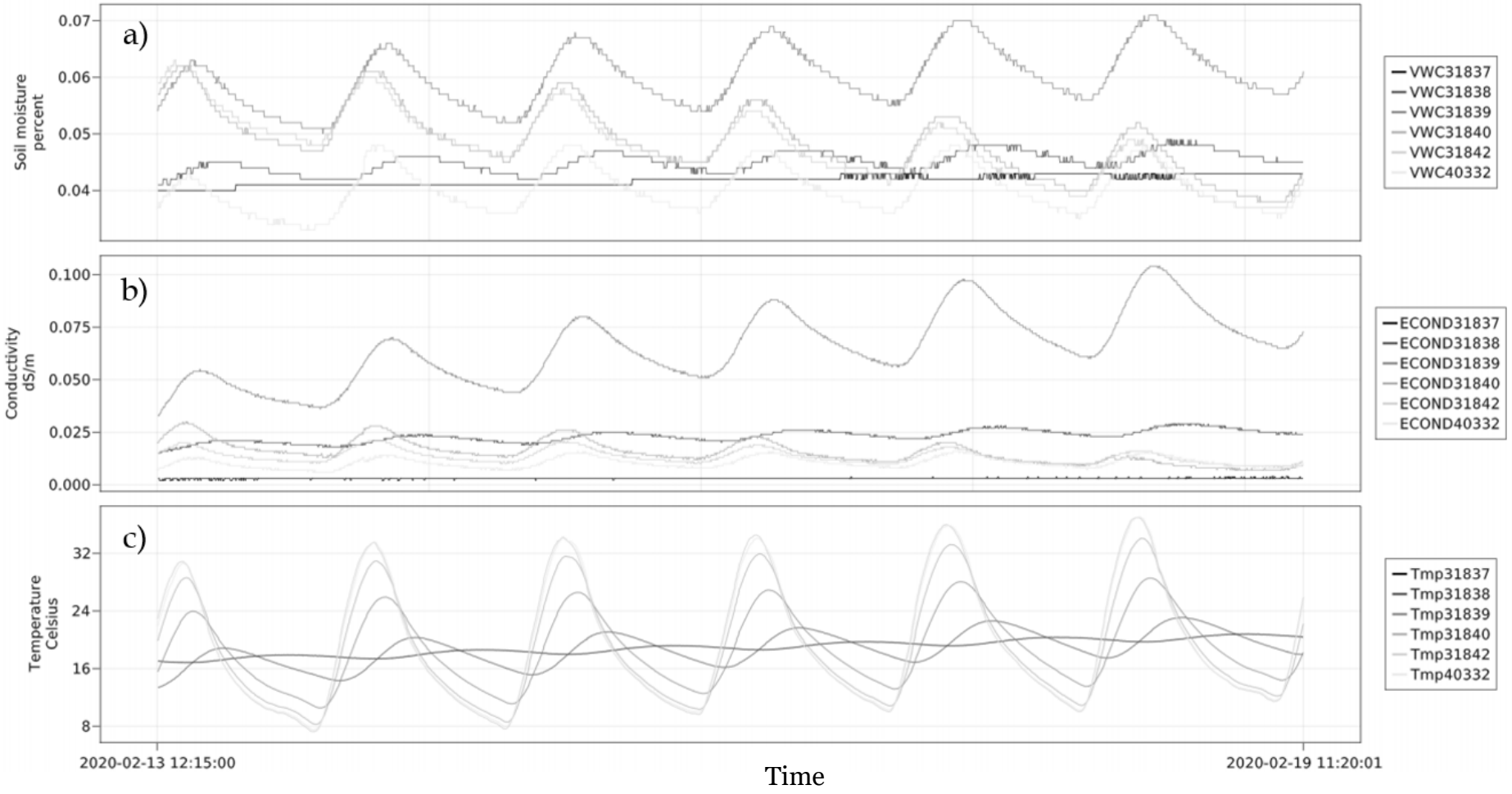

Some of these environmental variables, such as volumetric water content, soil electrical conductivity, and surface soil temperature, will play a critical role in the following sections in constructing the correlation matrix to quantify the environmental impact on sensor performance.

3.2 Qualitative image analysis

The focus of the current study is to identify environmental factors leading to an enhanced ability to identify and classify the various targets visible with IR imagery. Recall that the YPG study used three IR cameras, which we refer to as A310, MWIR, and LWIR, as discussed in Section 2. The A310 camera is utilized in both studies, while the MWIR and LWIR cameras are unique to the YPG data collection. To analyze target visibility, we compare target pixels to background pixels. The background is defined in terms of a specified area of interest (AOI) within the image that is generated from removing target correlated pixels from the whole test plot. The targets under consideration are identical as those in the CRREL study (orange objects in 16).

Figure 16. A310 image over the test plot at YPG (radiance values normalized to 255).

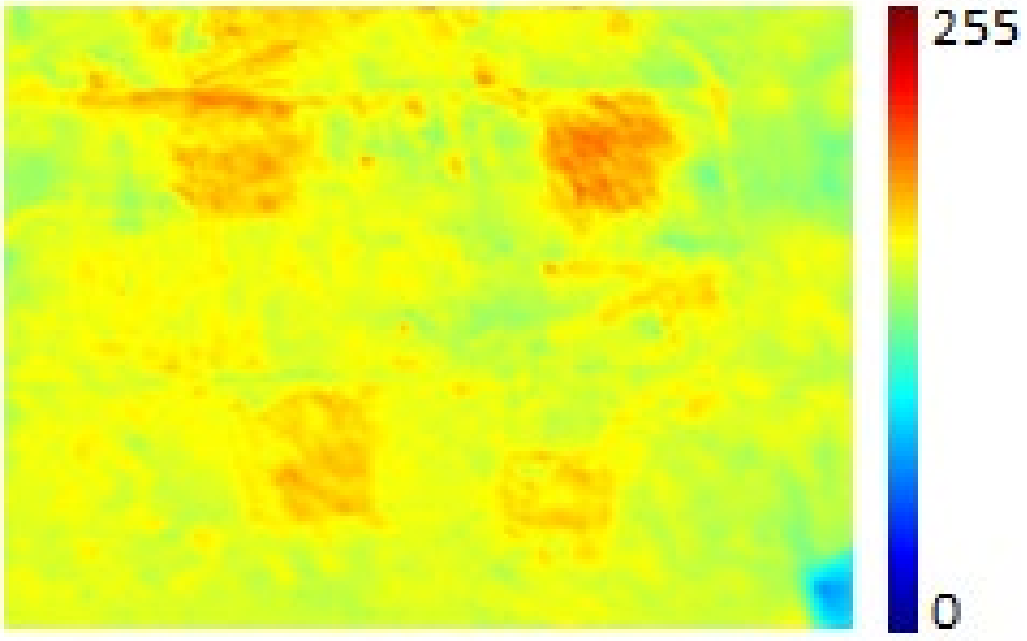

We use the following abbreviations throughout the remainder of the document to denote the four buried objects: pd (plastic deep), ps (plastic shallow), md (metal deep), and ms (metal shallow). In addition to these

four targets, Target 52 is included in this YPG AOI. This target was placed in the lane by YPG in 2014 and is a large plastic object buried at 15.24 cm.

Visibility comparisons are based on differences in mean pixel radiance (target minus background) for the A310 camera and color distance for the MWIR and LWIR cameras. The color distance used for this analysis is described in Sharma et al. (2005).

For an appreciation of the visibility comparisons we refer to Figure 17, which shows a snapshot of images from the three cameras in the context of the duration of the study.

In addition, environmental data (solar radiation (Figure 17a) and soil moisture (Figure 17c), are included as three time series plots corresponding to each system. These time series estimate target visibilities for each camera and target. The black vertical lines in Figures 17*d*, *f*, and *h* denote when the camera images were taken (1250), and the legends for the A310, MWIR, and LWIR plots include specific values to analyze visibility.

The A310 legend has a number for each target indicating the difference between the mean of the target and background pixels. For example, the plastic shallow pixels have a mean radiance that is 116.62 units above the mean radiance of the background's value of 21326.99 (Figure 17*e*). Target 52, on the other hand, has a mean radiance that is 332.12 units below the background's mean.

The MWIR and LWIR legends have a positive number for each target since the color distance is always non-negative. The mean of each background color channel is shown above each MWIR and LWIR AOI (Figures 17g and i). For example, the background means of the three-color channels (red, green, blue) of the three-band multi-spectral LWIR image are 0.808, 0.160, and 0.363, respectively. Continuing with the LWIR camera, the metal shallow target has a mean color distance (computed using Sharma et al. (2005)) of 18.394 units compared to the background mean color.

Figure 17. A snapshot of the YPG images that depicts (a) incoming (SR01Up) and reflected (SR01Dn) shortwave radiation in W/m², (b) timestamp with sun orientation, (c) volumetric water content (VWC[sensor#]) in percent, (d) A310 camera radiance difference (greyscale) over each target, (e) A310 camera image of test plot and individual target, (f) MWIR camera color distance over each target, (g) MWIR camera image of test plot and individual target, (h) LWIR color distance over each target, and (i) LWIR camera image of test plot and individual target. This format will be used in the following figures.

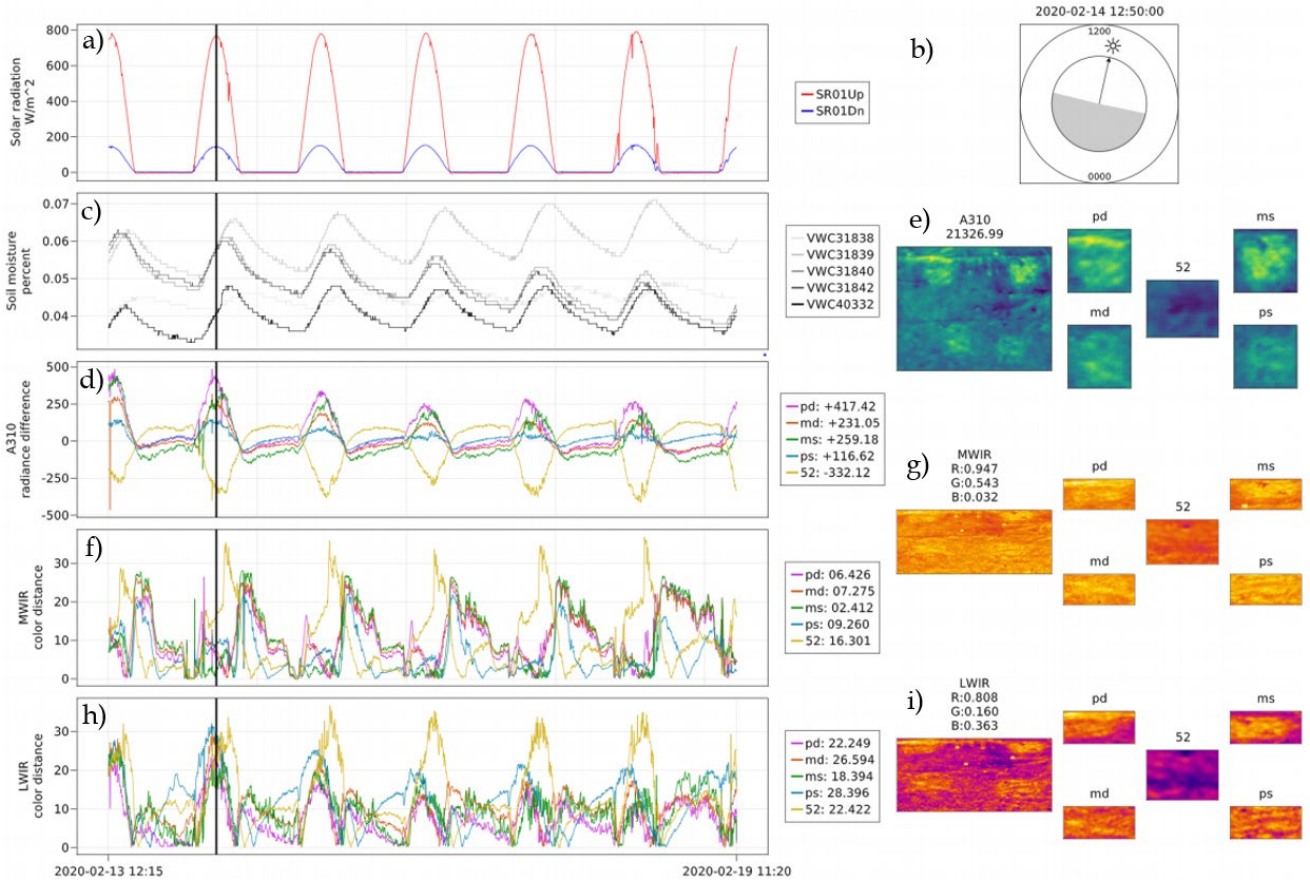

All three cameras follow a similar pattern with peaks occurring on approximately the same timescale with Target 52 displaying the largest contrast (Figures 17*d*, *f*, and *h*). Due to color distance being positive definite, the peak from the A310 is reversed. Interestingly, the directionality of the thermal crossover behavior with Target 52 is also reversed (plot derivative) and is observed throughout this analysis. A multitude of factors can contribute to this phenomenon. Since Target 52 was buried and left undisturbed prior to this study, the lack of soil disturbance and thus heterogeneity affected the heat and diffusion parameters of the soil differently. In addition, Target 52's innards are made up of a high explosive material, as opposed to the lawn fertilizer and YPG soil mixture of CRREL's four targets

The images for all three cameras appear to capture the thermal crossover phenomena (Paul et al. 2003) to varying degrees when the zero is intercepted or passed (Figure 17*d*, *f*, and *h*). Thermal crossover occurs twice or more each day and is the period when the object's thermal temperature is the same as the background's soil, resulting in the object's opaqueness. This behavior usually occurs under low light conditions, most commonly in the morning and evening, and is dependent both on the buried object's thermal inertia and environment. On the other hand, target visibility is most profound near solar noon, especially when incoming solar radiation exceeds 900 W/m^2. The behavior of target visibility following the trends in solar radiation is expected but also warrants further investigation. To analyze this trend, we focus on three points during the daily cycle, namely dawn, peak solar radiation, and dusk. A comparison of images collected at dawn is shown in Figure 18.

Figure 18. Comparison of selected environmental variables and images at dawn from CRREL—(a) incoming solar radiation (W/m²), (b) timestamp and sun orientation, (c) soil moisture (%), (d) Area of Interest radiance difference, (e) thermal IR image for test plot, and (f) thermal image of target Area of Interest; and YPG—(g) incoming solar radiation (W/m²), (h) timestamp and sun orientation, (i) soil moisture (%), (j) Area of Interest A310 radiance difference, (k) A310 thermal IR image for test plot and targets, (l) Area of Interest MWIR color distance, (m) MWIR thermal image of test plot and targets, (n) Area of Interest LWIR color distance, and (o) LWIR thermal image of test plot and targets.

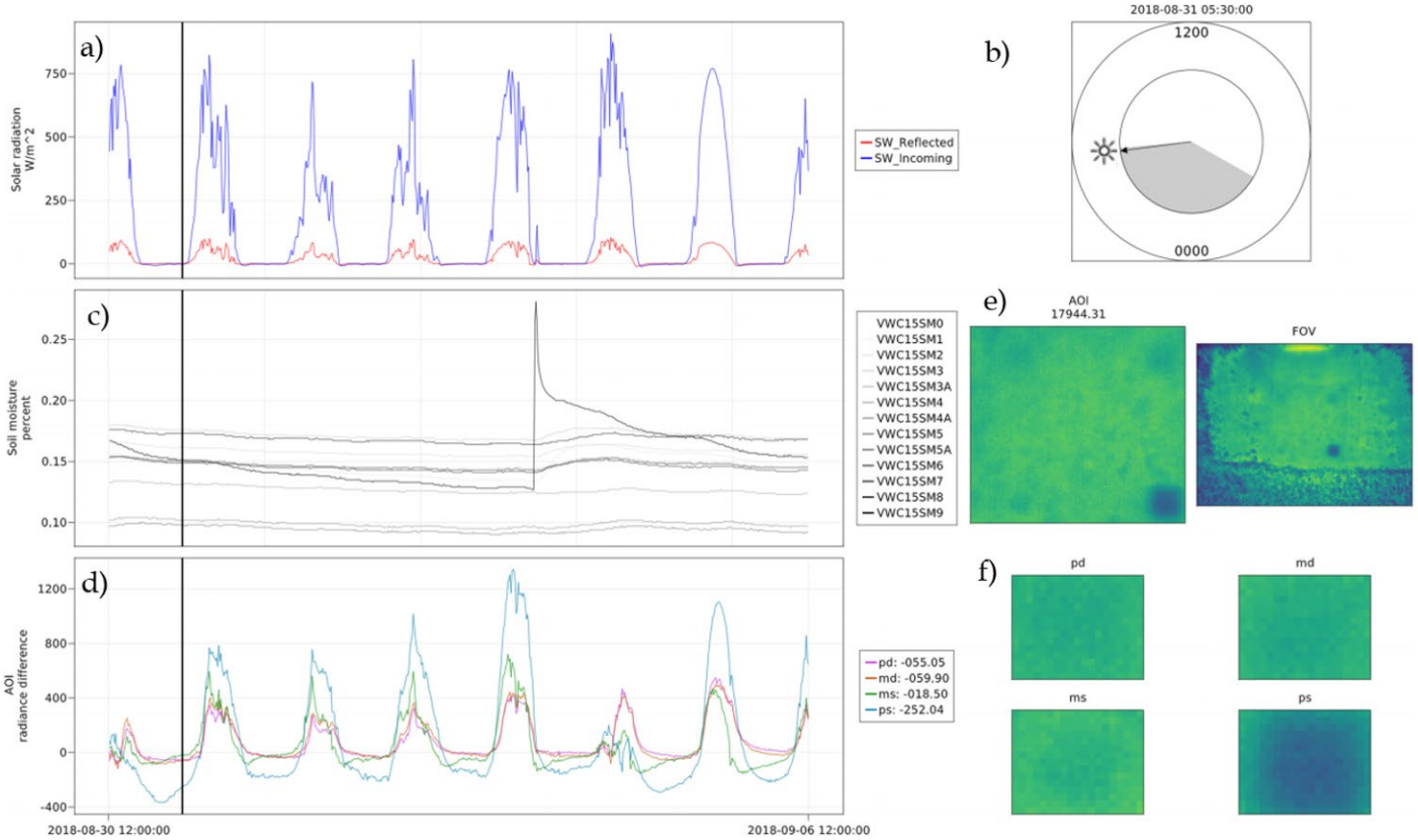

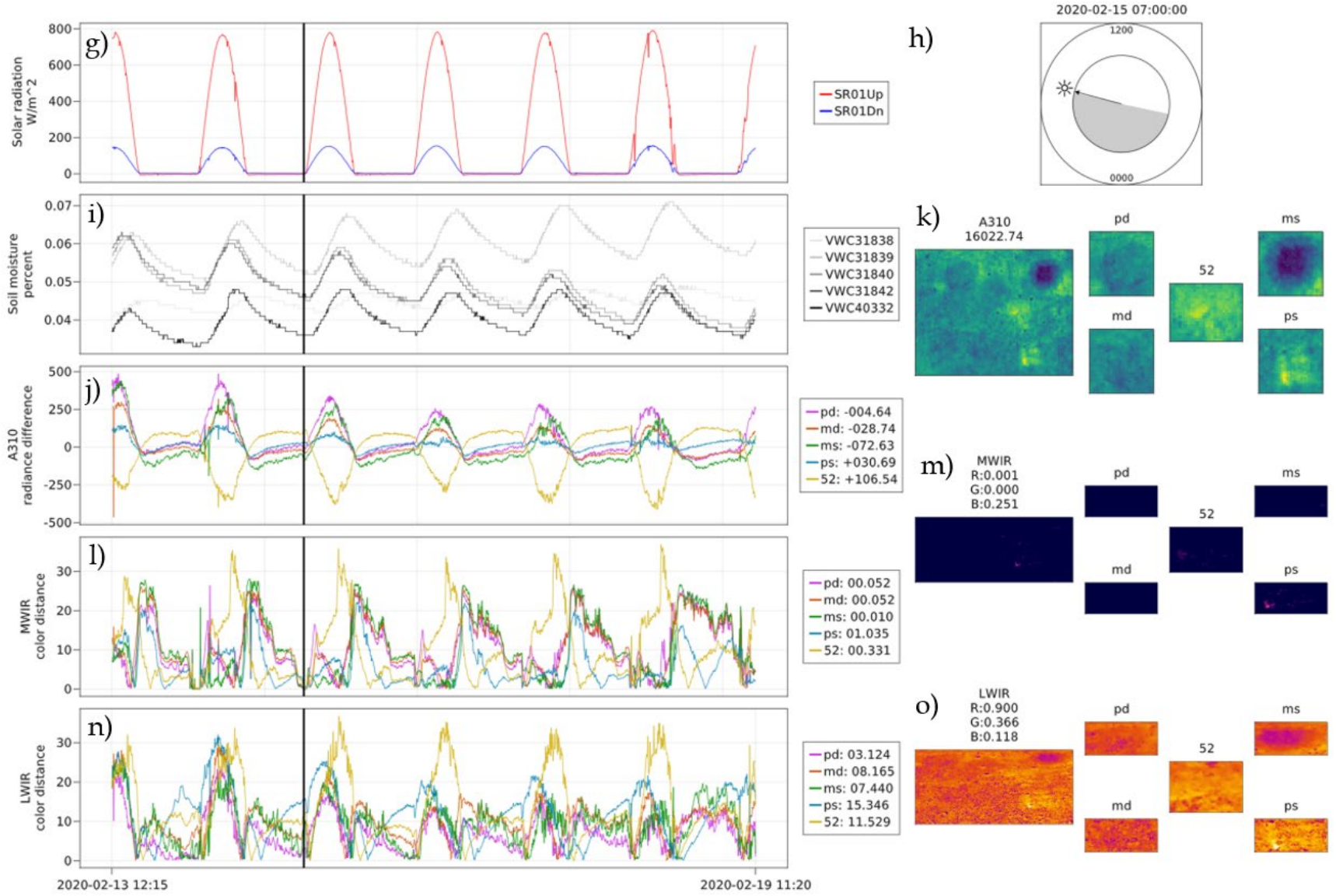
g)
Solar radiation W/m^2
800
600
400
200
0
SR01Up
SR01Dn
h)
2020-02-15 07:00:00
1200
0000
i)
Soil moisture percent
0.07
0.06
0.05
0.04
VWC31838
VWC31839
VWC31840
VWC31842
VWC40332
k)
A310
16022.74
pd
ms
52
md
ps
j)
A310 radiance difference
500
250
0
-250
-500
pd: -004.64
md: -028.74
ms: -072.63
ps: +030.69
52: +106.54
m)
MWIR
R:0.001
G:0.000
B:0.251
pd
ms
52
md
ps
l)
MWIR color distance
30
20
10
0
pd: 00.052
md: 00.052
ms: 00.010
ps: 01.035
52: 00.331
o)
LWIR
R:0.900
G:0.366
B:0.118
pd
ms
52
md
ps
n)
LWIR color distance
30
20
10
0
pd: 03.124
md: 08.165
ms: 07.440
ps: 15.346
52: 11.529
2020-02-13 12:15
2020-02-19 11:20

The top plot is from the CRREL site, and the bottom plot is from YPG. In both sets of images, we see that the plastic targets have higher mean radiance values at dawn, but the YPG results are less pronounced in comparison to the CRREL data. The metal shallow target is more readily visible at YPG at dawn versus at CRREL. The deep targets, on the other hand, have poor visibility in both data sets. Like Figure 17, the YPG Target 52 tends to have the best visibility out of the five main targets, and although its thermal image looks like the plastic shallow object, Target 52 appears to have thermal crossover behavior reversed from the rest. Lastly, when we look at the MWIR images at dawn, hardly any of the targets are visible. In contrast, the LWIR images follow similar behavior to that of the A310, where the shallow targets and Target 52 are distinctly visible.

Figure 19 compares images from CRREL and YPG at dusk. At dusk the behavior is reversed as thermal crossover occurs in the opposite direction (i.e., radiance difference and color distance plots sloping downwards). The plastic shallow target in the A310 camera view shows a significant decrease in magnitude at YPG as compared to CRREL. Similar as before, Target 52 at YPG displays the largest contrast, with opposite thermal crossover behavior. The target visibility with the MWIR camera improves, with optimal performance discovered to be in the early evening hours after dusk.

A comparison of images occurring at peak solar radiation is shown in Figure 20.

Figure 19. Comparison of selected environmental variables and images at dusk from CRREL—(a) incoming solar radiation (W/m²), (b) timestamp and sun orientation, (c) soil moisture (%), (d) Area of Interest radiance difference, (e) thermal IR image for test plot, and (f) thermal image of target Area of Interest; and YPG—(g) incoming solar radiation (W/m²), (h) timestamp and sun orientation, (i) soil moisture (%), (j) Area of Interest A310 radiance difference, (k) A310 thermal IR image for test plot and targets, (l) Area of Interest MWIR color distance, (m) MWIR thermal image of test plot and targets, (n) Area of Interest LWIR color distance,and (o) LWIR thermal image of test plot and targets.

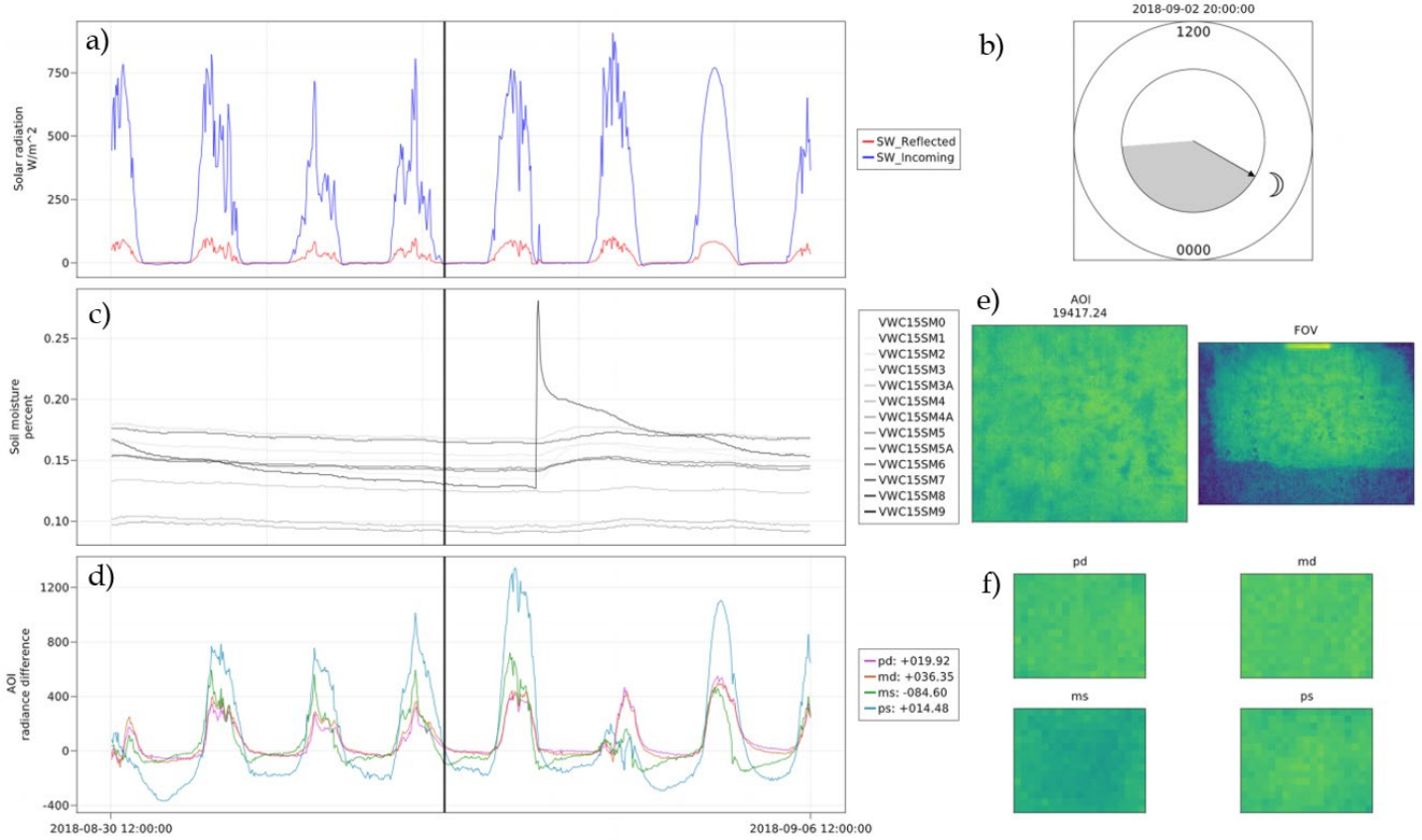

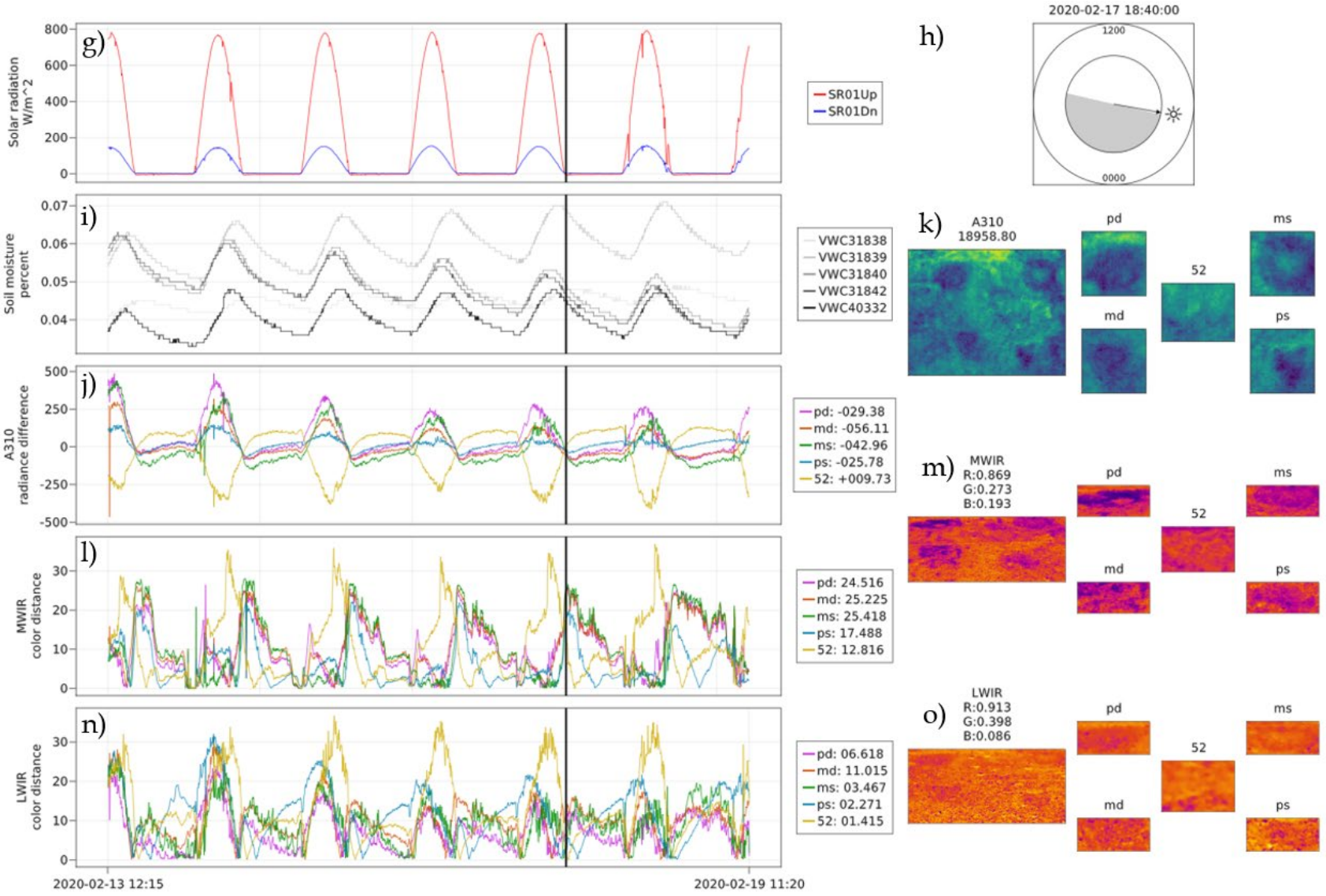
g)
Solar radiation W/m^2
800
600
400
200
0
SR01Up
SR01Dn
h)
2020-02-17 18:40:00
1200
0000
i)
Soil moisture percent
0.07
0.06
0.05
0.04
VWC31838
VWC31839
VWC31840
VWC31842
VWC40332
k)
A310
18958.80
pd
ms
52
md
ps
j)
A310 radiance difference
500
250
0
-250
-500
pd: -029.38
md: -056.11
ms: -042.96
ps: -025.78
52: +009.73
m)
MWIR
R:0.869
G:0.273
B:0.193
pd
ms
52
md
ps
l)
MWIR color distance
30
20
10
0
pd: 24.516
md: 25.225
ms: 25.418
ps: 17.488
52: 12.816
n)
LWIR color distance
30
20
10
0
pd: 06.618
md: 11.015
ms: 03.467
ps: 02.271
52: 01.415
o)
LWIR
R:0.913
G:0.398
B:0.086
pd
ms
52
md
ps
2020-02-13 12:15
2020-02-19 11:20

Figure 20. Comparison of selected environmental variables and A310 images at peak solar radiation at CRREL—(a) incoming solar radiation (W/m²), (b) timestamp and sun orientation, (c) soil moisture (%), (d) Area of Interest radiance difference, (e) thermal IR image for test plot, and (f) thermal image of target Area of Interest; and YPG—(g) incoming solar radiation (W/m²), (h) timestamp and sun orientation, (i) soil moisture (%), (j) Area of Interest A310 radiance difference, (k) A310 thermal IR image for test plot and targets, (l) Area of Interest MWIR color distance, (m) MWIR thermal image of test plot and targets, (n) Area of Interest LWIR color distance, and (o) LWIR thermal image of test plot and targets.

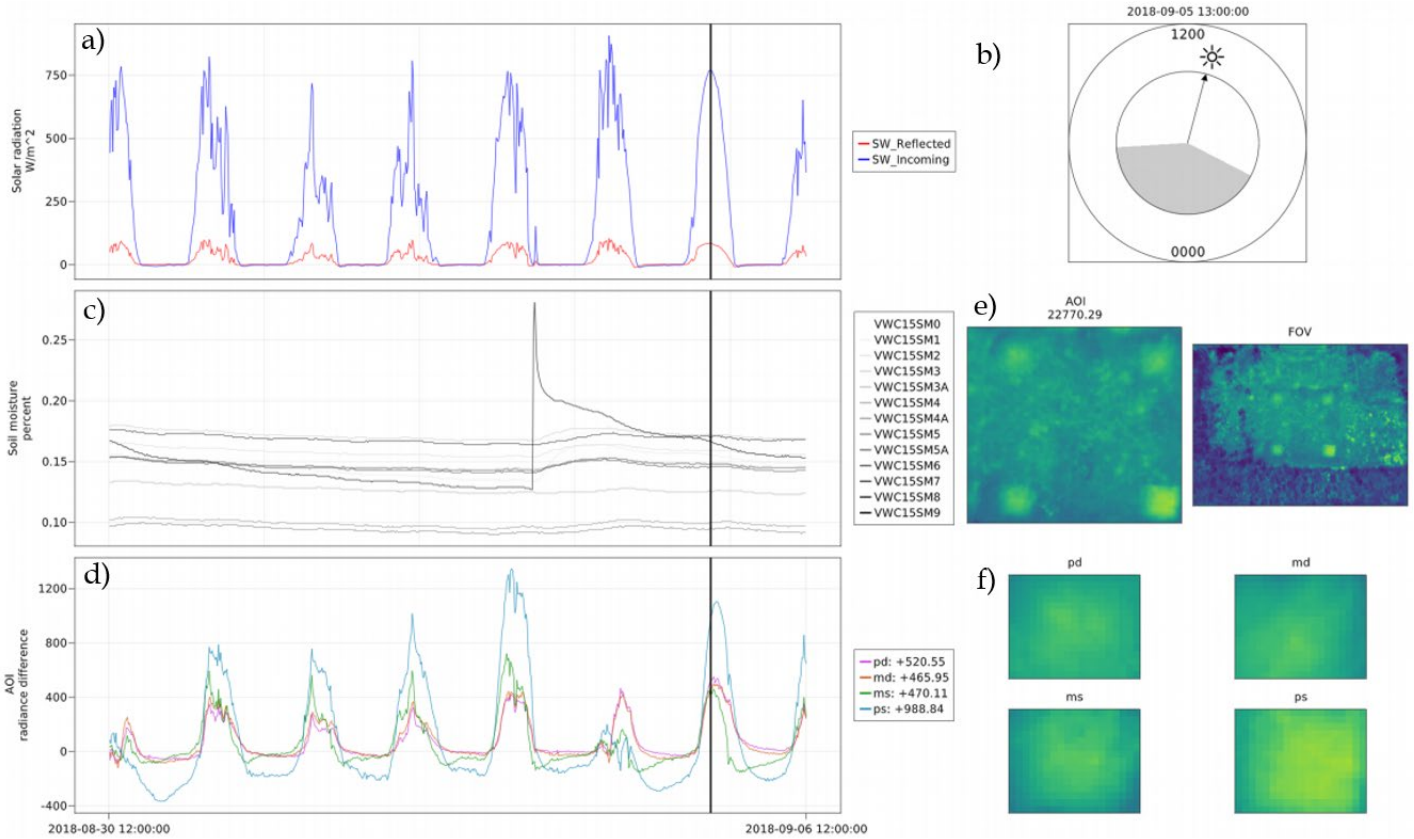

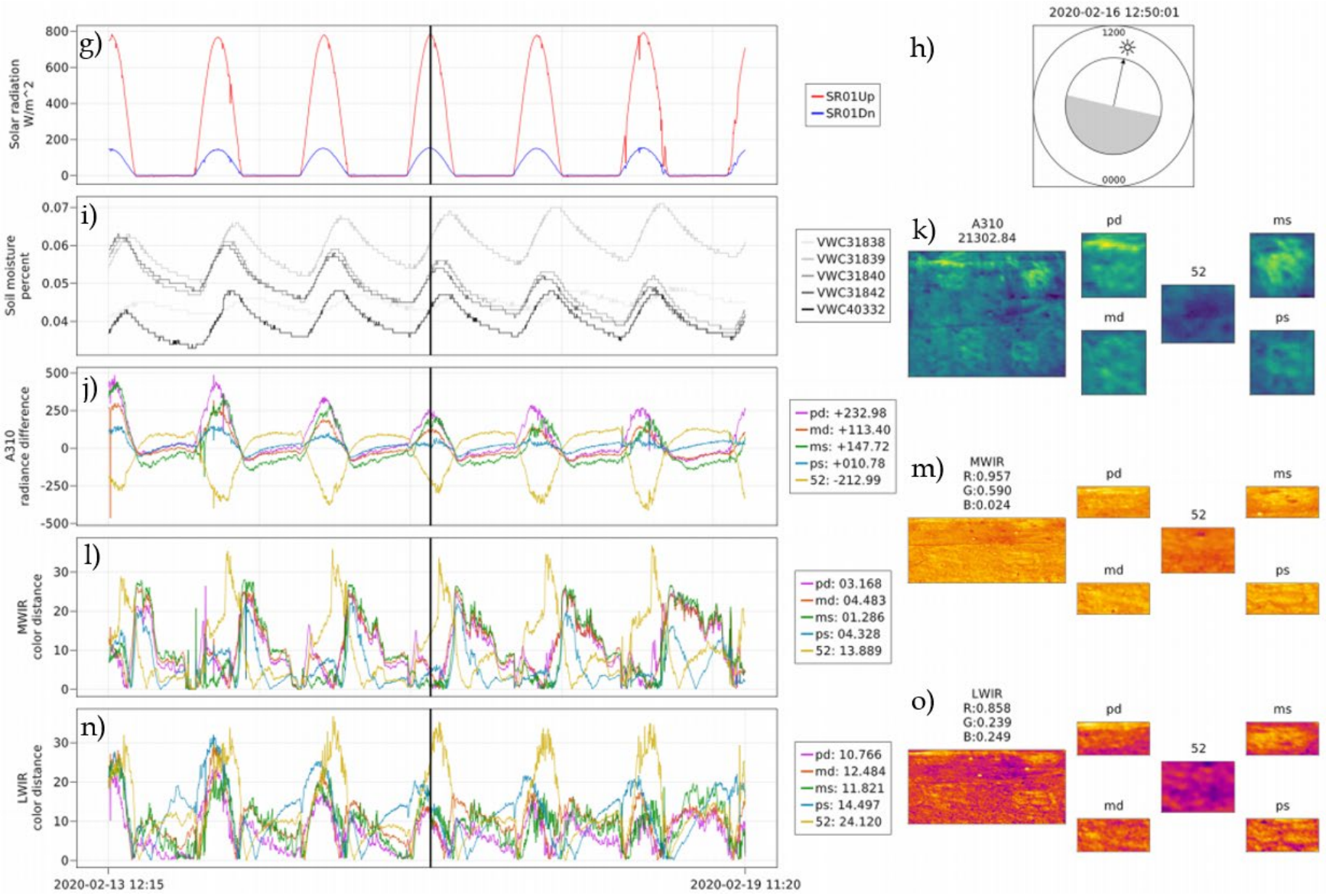
g)
Solar radiation W/m^2
800
600
400
200
0
SR01Up
SR01Dn
h)
2020-02-16 12:50:01
1200
0000
i)
Soil moisture percent
0.07
0.06
0.05
0.04
VWC31838
VWC31839
VWC31840
VWC31842
VWC40332
k)
A310
21302.84
pd
md
52
ms
ps
j)
A310 radiance difference
500
250
0
-250
-500
pd: +232.98
md: +113.40
ms: +147.72
ps: +010.78
52: -212.99
m)
MWIR
R:0.957
G:0.590
B:0.024
l)
MWIR color distance
30
20
10
0
pd: 03.168
md: 04.483
ms: 01.286
ps: 04.328
52: 13.889
o)
LWIR
R:0.858
G:0.239
B:0.249
n)
LWIR color distance
pd: 10.766
md: 12.484
ms: 11.821
ps: 14.497
52: 24.120
2020-02-13 12:15
2020-02-19 11:20

Unsurprisingly, targets at the CRREL test plot possess higher visibility than those at YPG. During peak solar input, according to the color difference plots, the LWIR camera has a higher tendency to outperform the MWIR camera for target detection. The contrast in visibilities between both sites is expected due to the difference in soil type and VWC. Unlike the YPG test plot, the soil at the CRREL's test plot was excavated, homogenized, and then replaced during target emplacement. The grainsize distribution at CRREL corresponds to a silty sand with an average dry density of 1883.47 kg/m^3. YPG's soil, on the other hand, is loamy with a high concentration of calcium carbonate, salt, and clay (Hausner et al. 2019). The average soil density at the 5 cm depth measured at YPG is approximately 1773 kg/m^3. Finally, CRREL is in a temperate, deciduous forest biome, whereas YPG is in a desert.

3.3 Quantitative environmental effects

The effect of various environmental phenomological features on target visibility is next explored. Recall that we define target visibility by comparing mean pixel values between a specified target and background (with target pixels removed). To conduct this analysis, we model the visibility of each target with respect to the nine environmental variable inputs summarized in Table 1. The variables for VWC and electrical conductivity (ECOND) are computed from averaging sensor readings from the CS655 sensors. To compute VWC at a given instance, the CS655 soil moisture readings near the surface are averaged. Similarly, to compute ECOND at a given instance, the CS655 conductivity readings near the surface are averaged. Correlations between the nine environmental variables are shown in Figure 21 (YPG) and Figure 22 (CRREL).

Figure 21. Correlations for YPG environmental data. Dark blue represents high correlation, whereas yellow denotes poor correlation.

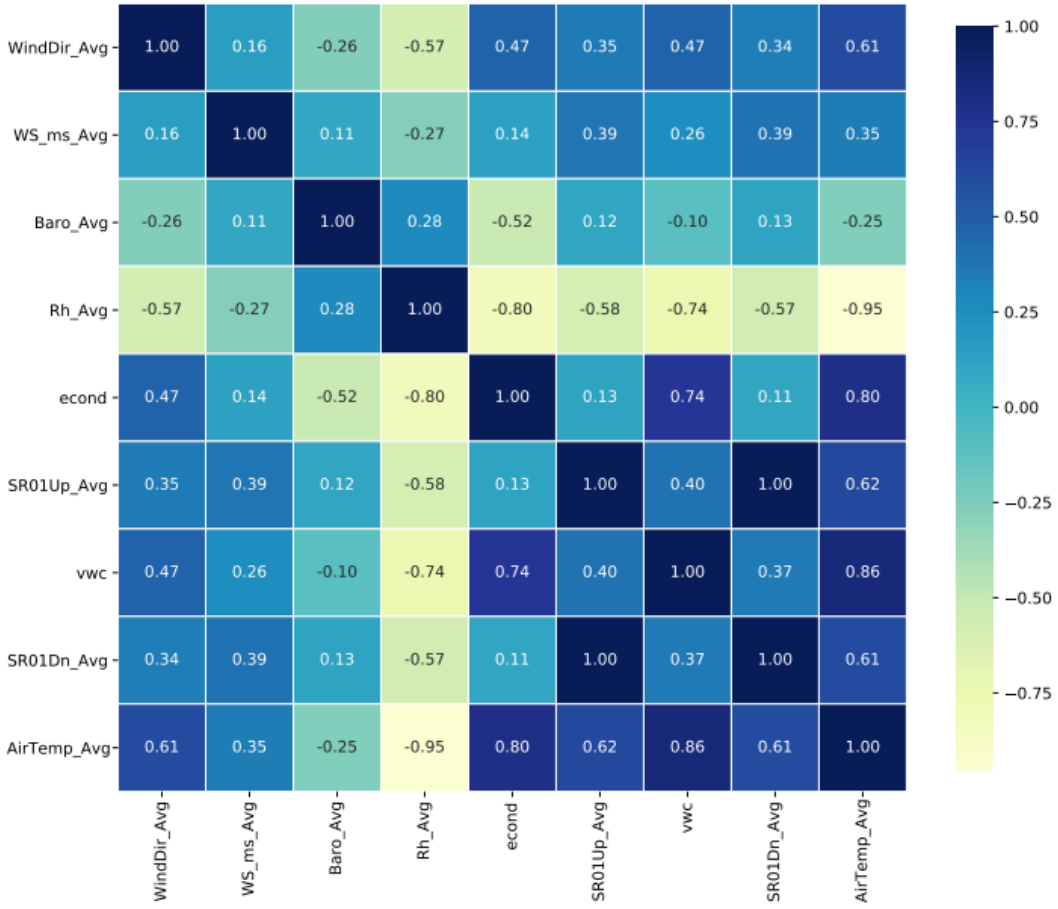

Figure 22. Correlations for CRREL environmental data. Dark blue represents high correlation, whereas yellow denotes poor correlation.

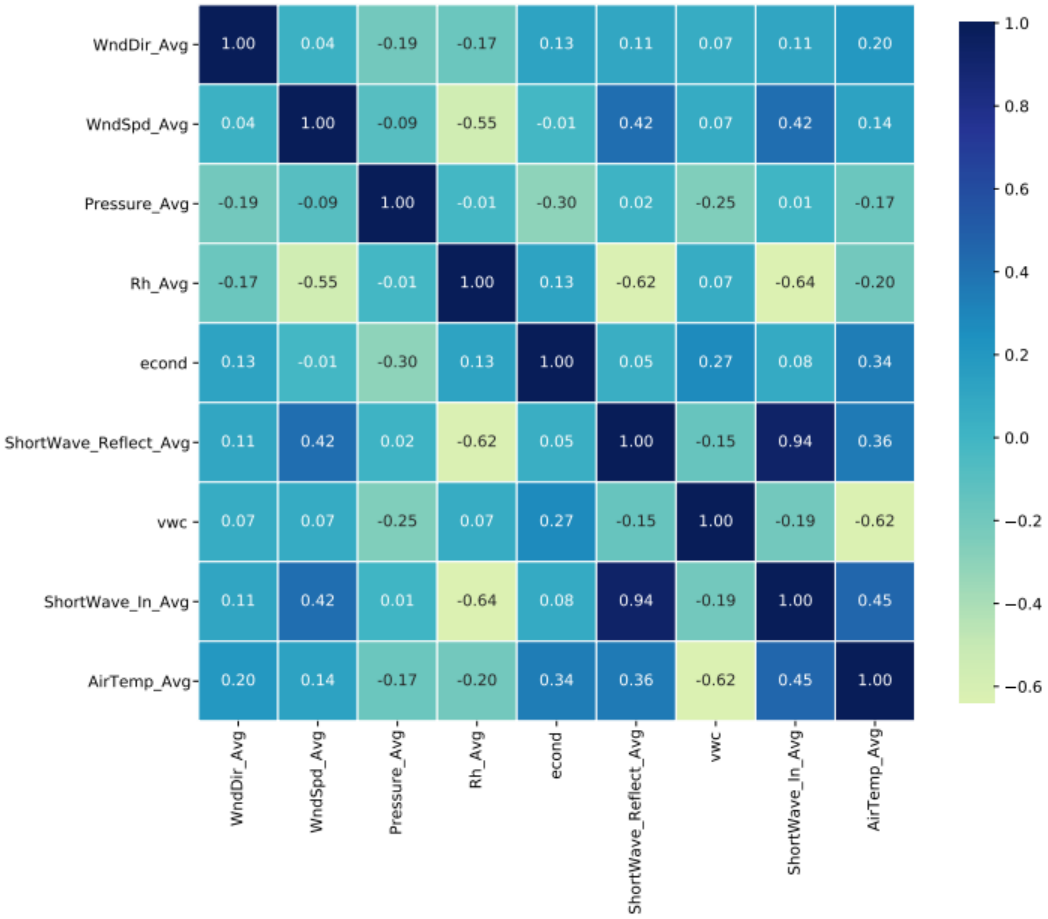

To measure the environmental effects of the nine input variables from Table 1, we use a nonlinear boosted tree model from Chen et al. (2016) to approximate a function mapping of these nine variables to visibility outputs for each target. These function approximations are then analyzed using Shapley Additive Explanations in Štrumbelj and Kononenko (2014), Lundberg and Lee (2017), Lundberg et al. (2020), and Lundberg et al. (2018) to determine how the environmental inputs affect the visibility outputs of the model for the A310 thermal IR camera. Shapley values provide a measure of feature importance in a local sense by additively decomposing an observed response into a sum of effects from each input variable with respect to a baseline effect.

Since this analysis depends on a specific target, we developed five models for the YPG data set (one for each of the five targets: ps, pd, ms, md, 52) and four models for the CRREL data set (one for each of the four targets: ps, pd, ms, md). This analysis is summarized in in the following figures.

To explain the meaning of the plots in these figures, we focus on Figure 23. This figure summarizes the environmental effects of the nine variables in Table 1 on the visibility of the plastic shallow target using the CRREL data set. In Figure 23*a* there is a feature importance plot with nine scatter plots below it (Figures 23*b–j*). The feature importance plot orders the input variables by their overall impact on (plastic shallow) target visibility (i.e. mean radiance difference between target and background pixels). Positive Shapley values indicate a positive effect on this radiance difference and negative Shapley values indicate a negative effect. Shapley values are measured in the model output units (mean radiance difference between target and background pixels). For example, in Figures 23*b–j*, the most important environmental input is the mean incoming shortwave radiation (Figure 23*b*).

Moreover, the coloring in the feature importance plot indicates that low values of mean incoming shortwave radiation negatively impact the radiance difference (by as much as 200 units), whereas high values of the mean incoming shortwave radiation positively impact the radiance difference (by as much as 500 units). The scatter plots further depict each input variable as well as second order interactions (multi-variables). For example, the scatter plot of Figure 23*b* analyzes mean incoming shortwave radiation. The observed values of the mean incoming shortwave radiation are compared against the Shapley value for that observation. This plot gives us some indication about which values of the mean incoming shortwave radiation positively and negatively affect the radiance difference.

In this example, values of mean incoming shortwave radiation above 200 W/m^2 have a positive impact on the radiance difference. The multi interactions are represented by the scatter plot color (located on the right-hand side of each scatter plot). For example, in the scatter plot for mean incoming shortwave radiation, the coloring indicates the observed VWC percentage as derived from the correlation matrix (Figure 24). Consider values of mean incoming shortwave radiation between 400 and 1,000 W/m^2, where there is an overall positive effect on radiance difference (positive Shapley values). However, for these values we can see a slight separation based on VWC coloring. We see that lower VWC (light blue) have higher Shapley values, and higher VWC values (dark blue) have lower Shapley values.

To organize the results of this analysis, we specify a target of interest and then compare environmental effects (using Shapley feature importance plots and scatter plots explained above) for that object between the CRREL and YPG data set.

Figure 23. Environmental effects for ps targets using CRREL data: (a) Shapley Additive Explanations value features importance plot for the nine environmental variables, and individual Shapley Additive Explanations value scatter plots for (b) incoming shortwave radiation (W/m²), (c) reflected shortwave radiation (W/m²), (d) air temperature (°C), (e) volumetric water content (%), (f) electrical conductivity (dS/cm²), (g) relative humidity (%), (h) atmospheric pressure (mb), (i) windspeed (cm/s), and (j) wind direction (degrees). This format will be used in the following figures.

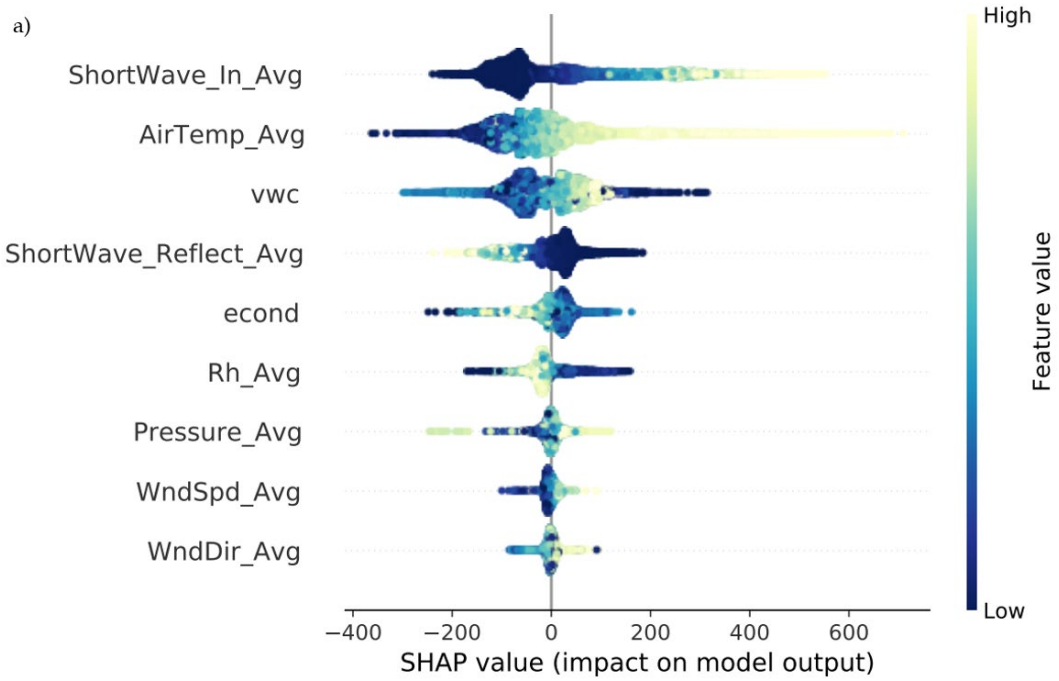

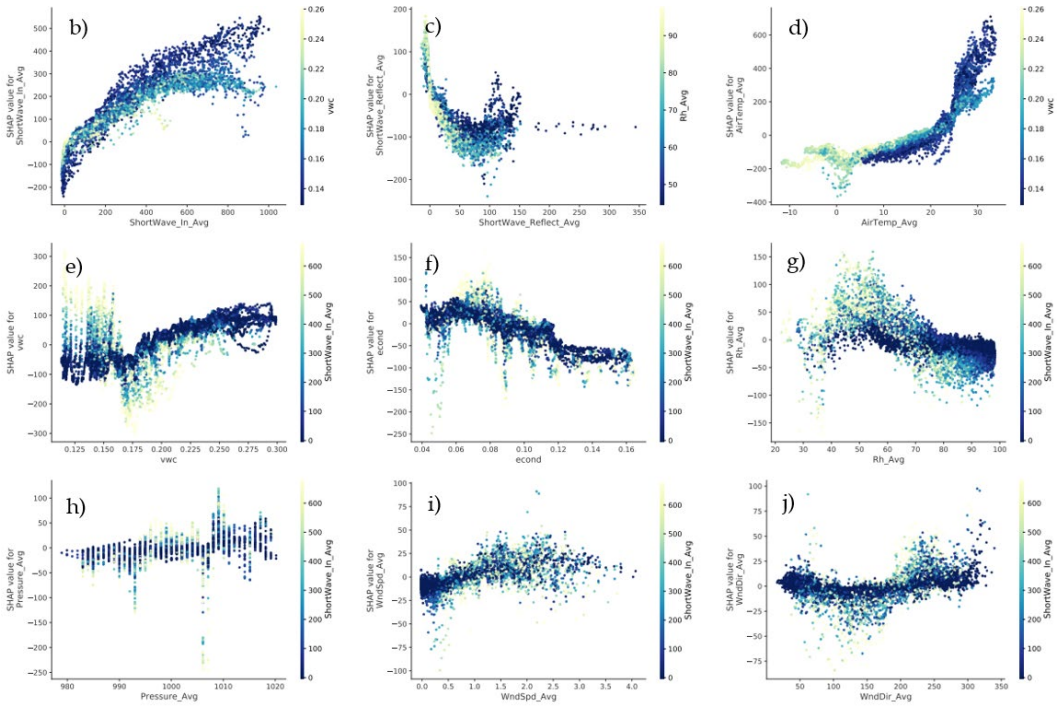

We start by analyzing the ps targets. Figure 23 and Figure 24 summarize the environmental effects on the plastic shallow object visibility through a comparison of the CRREL and YPG data sets. Solar loading is observed to be the most important environmental phenomenology feature for both sites, where increased solar radiation tends to increase the radiance difference. Volumetric water content of the soil is also important for both sites, where higher soil moisture levels tend to result in lower Shapley values, as observed in the correlation matrix in Figure 21 and Figure 22. In contrast, air temperature appears to be an important feature only for the CRREL data set, while the rest of the environmental variables do not strongly affect the radiance difference of the plastic shallow targets. This finding is unsurprising due to the higher levels of humidity at CRREL in late-Spring to mid-Summer when the data set was collected at Hanover in comparison to the dryer climate at YPG in February.

Figure 24. Environmental effects for ps targets using the A310 camera at YPG.

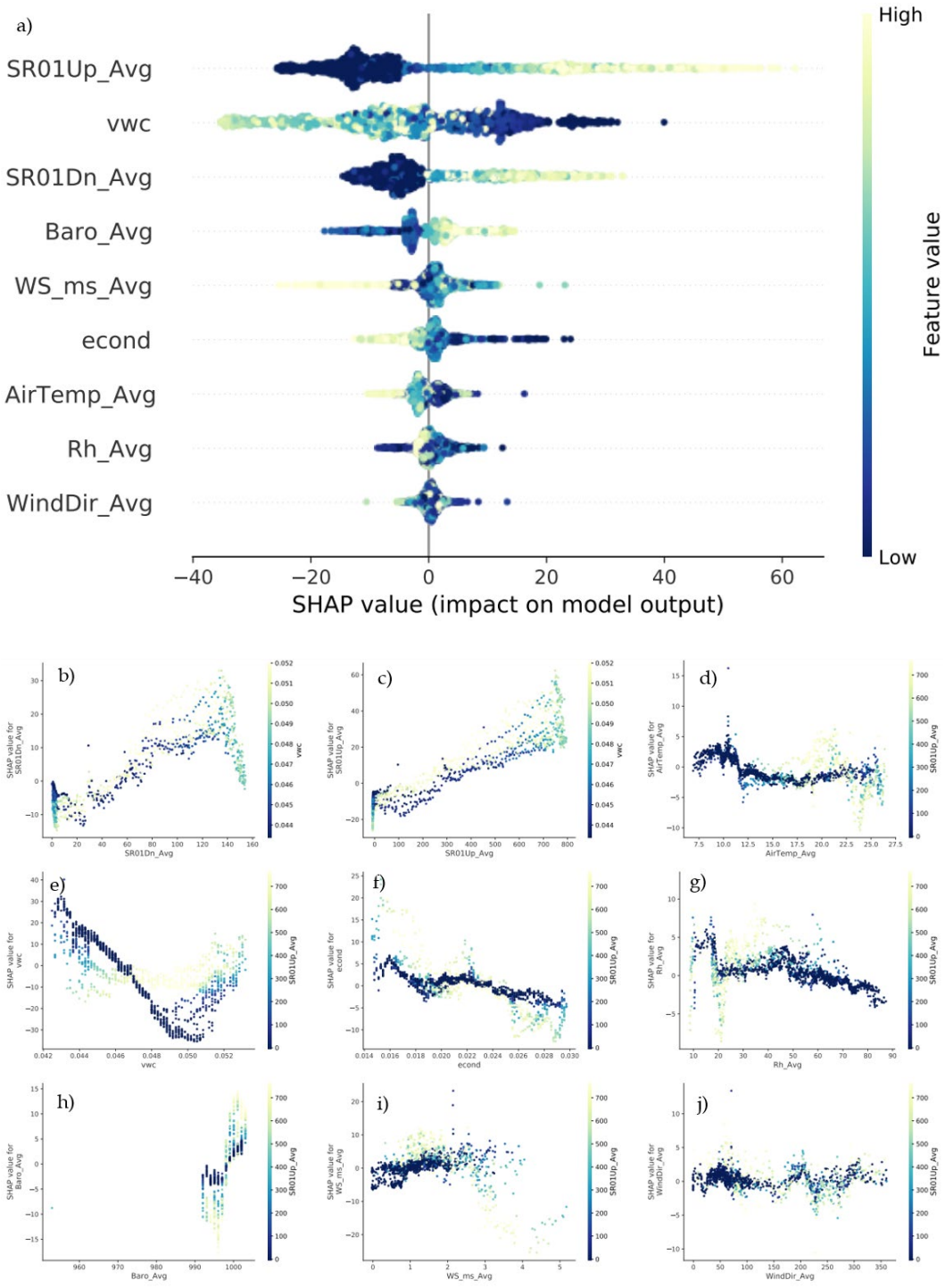

Figure 25 and Figure 26 summarize the environmental effects on the deep plastic buried object visibility for the CRREL and YPG data sets. In the CRREL data set, air temperature, soil moisture, and soil conductivity are the most important environmental features. At YPG, solar radiation and soil conductivity have the biggest influence on thermal radiance values. Air

temperature has a positive effect on radiance difference at CRREL but a negative effect at YPG, while soil conductivity has a negative effect at both sites. These differences can be explained by the difference in biomes.

Figure 25. Environmental effects for pd targets using CRREL data.

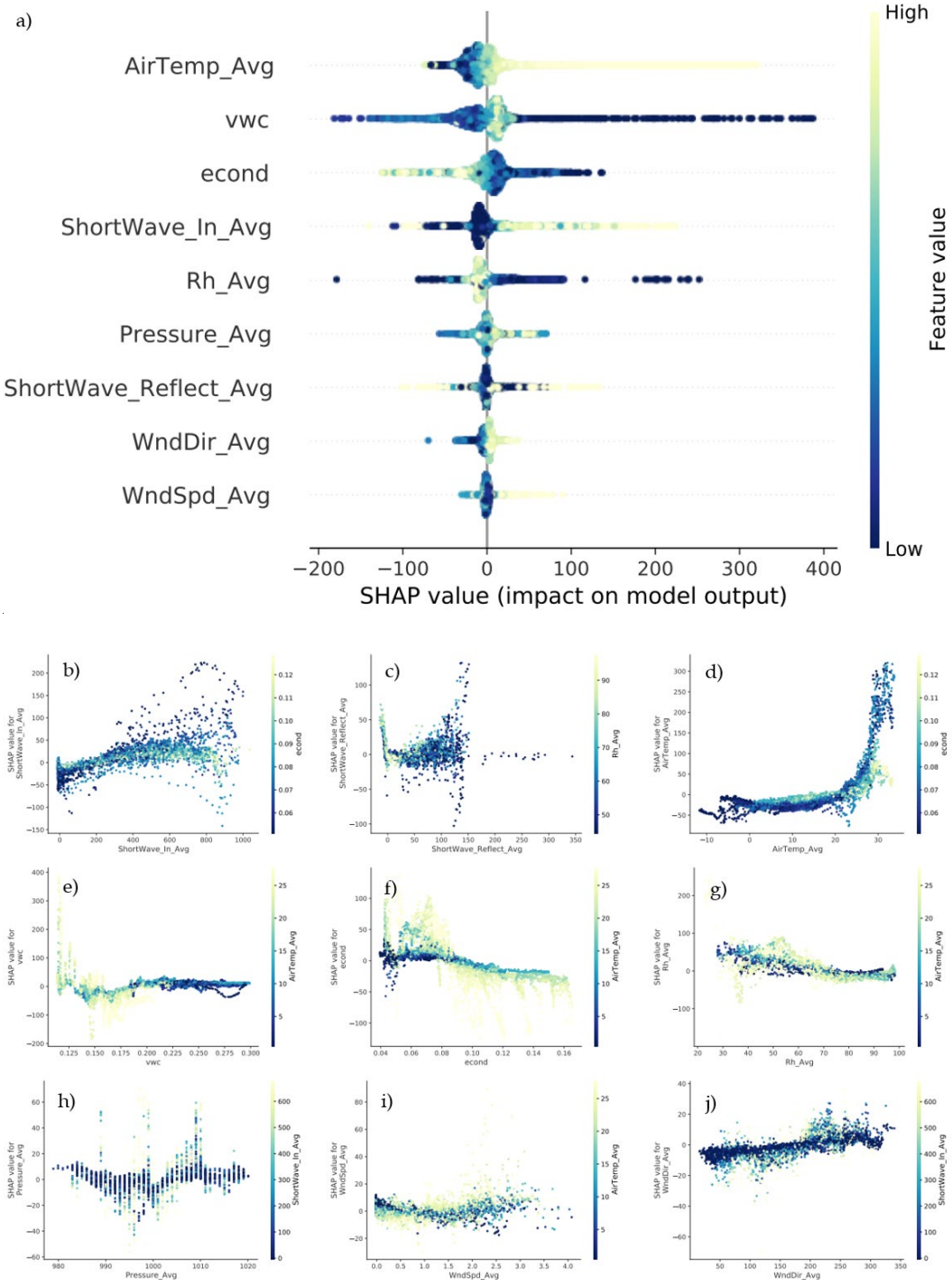

Figure 26. Environmental effects for pd targets using the A310 camera at YPG.

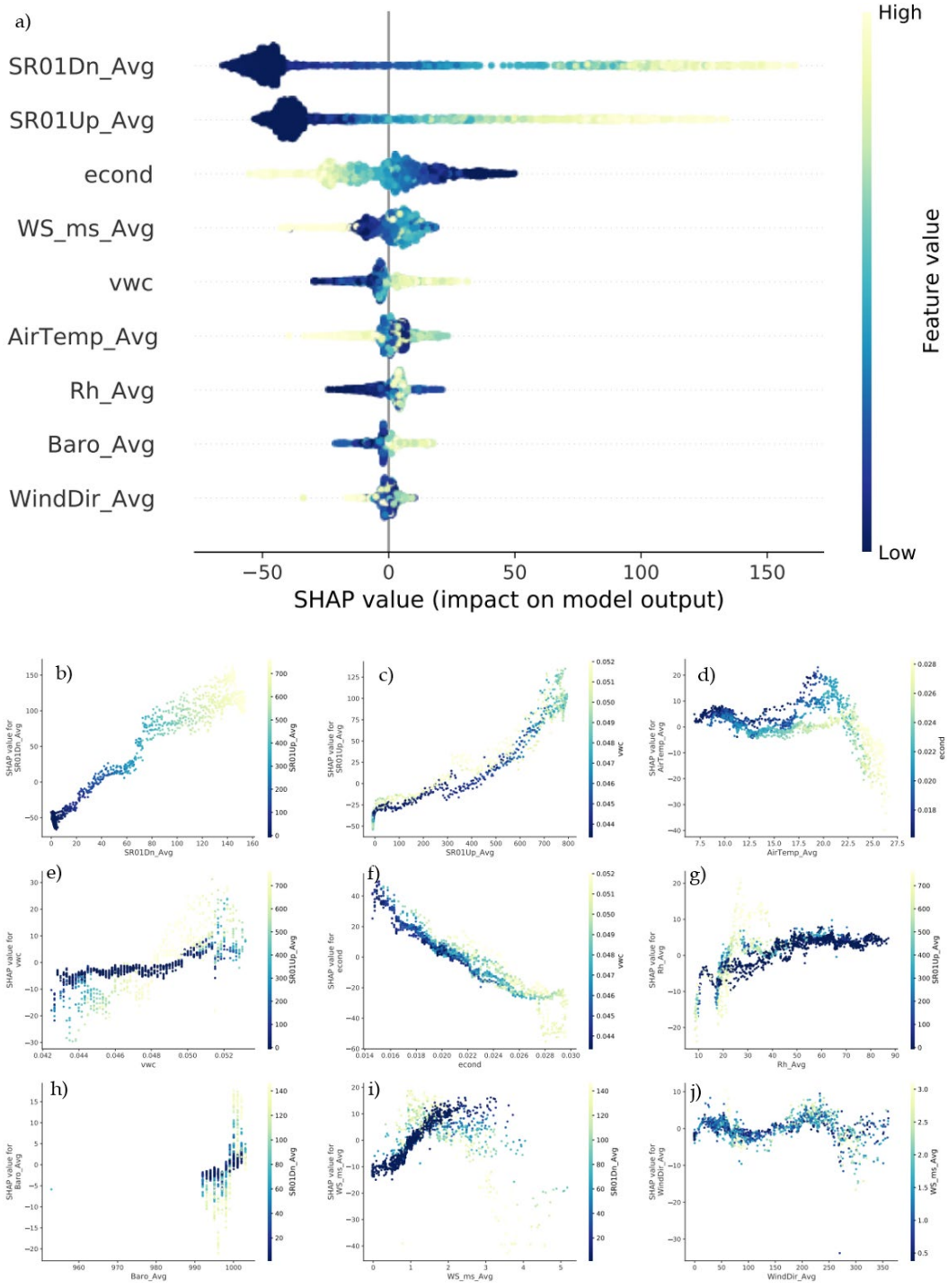

We now analyze md targets. Figure 27 and Figure 28 summarize the environmental effects on md targets for the CRREL and YPG data sets. In both data sets, solar radiation is the most important environmental feature. Additionally, higher conductivity and soil moisture tend to decrease the radiance difference at both sites, with the effect of

conductivity being more pronounced at YPG. From Figures 15a and b, we observed VWC increase with increasing ECOND, with a water content accuracy as high as ±3% at a conductivity of <10 dS/m. This result is expected due to the increase in soluble salt content found at that site, which affects the electric and magnetic field strength of propagating waves. Another contrast observed is in the CRREL data set, where higher air temperature leads to a positive effect on radiance difference. Increases in temperature allows for greater variability in the disrupted temperature flow of the soil surface.

Figure 27. Environmental effects for md targets using CRREL data.

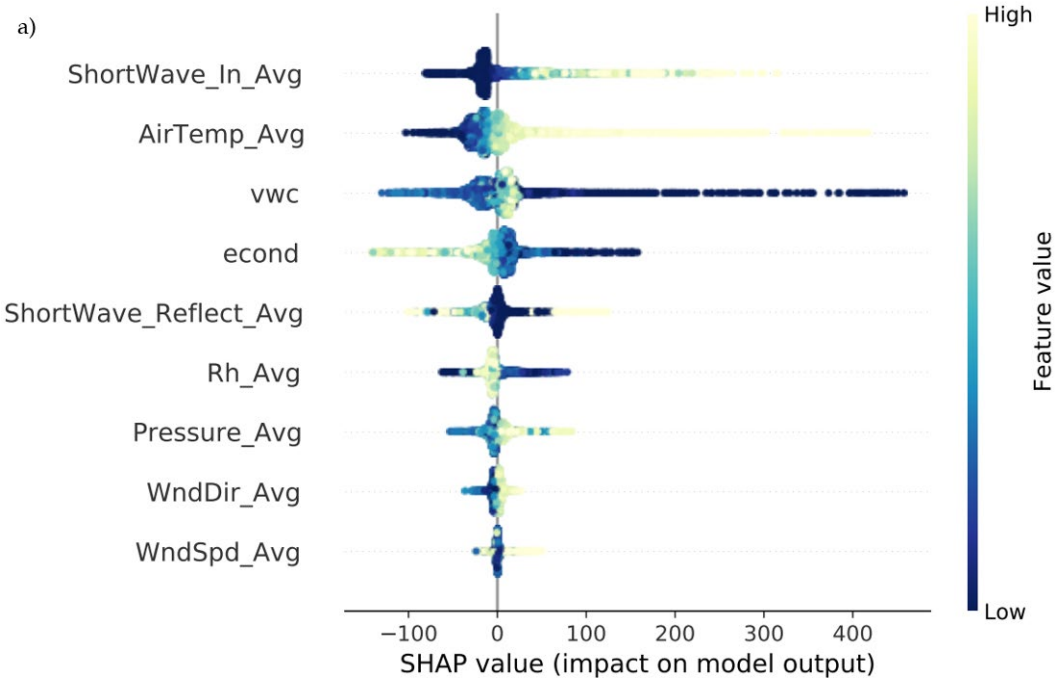

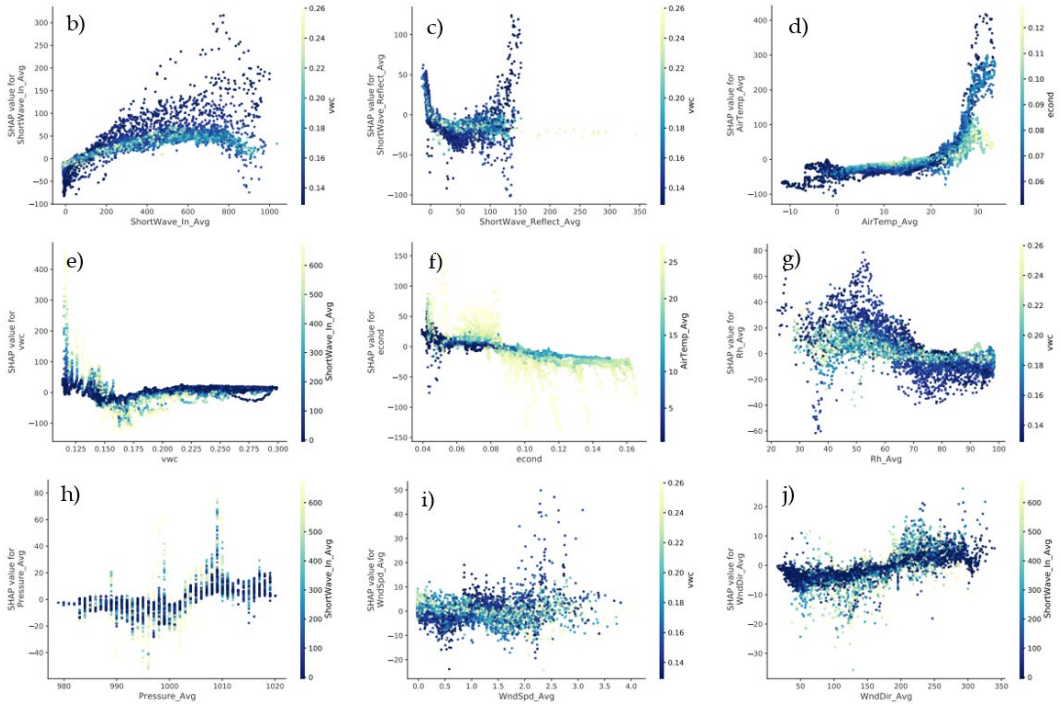

Figure 28. Environmental effects for md targets using the A310 camera at YPG.

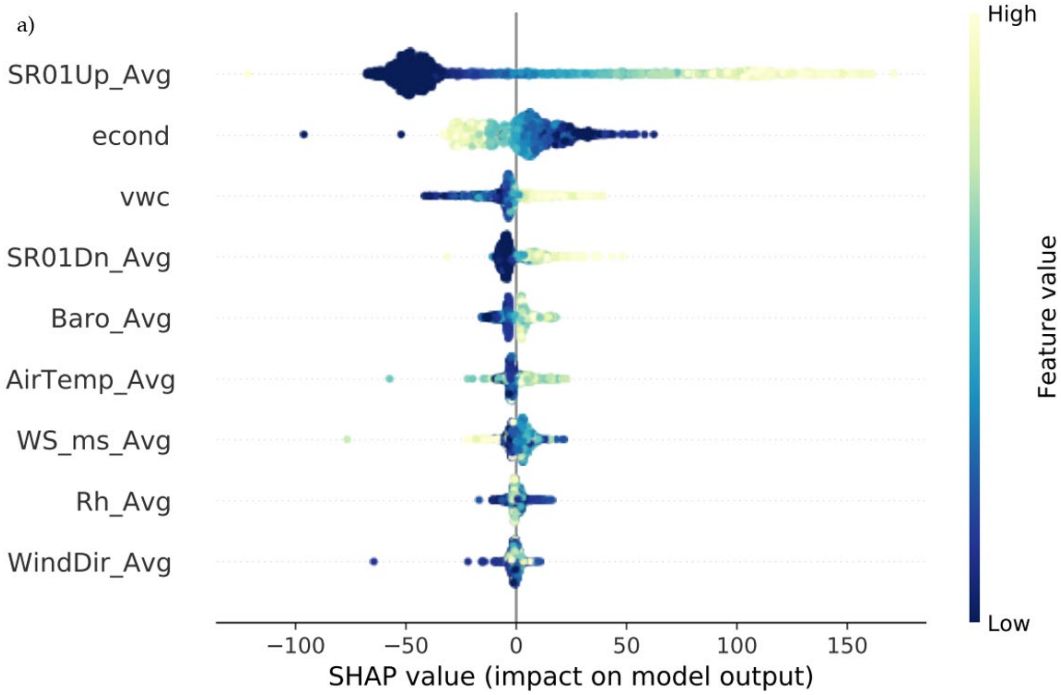

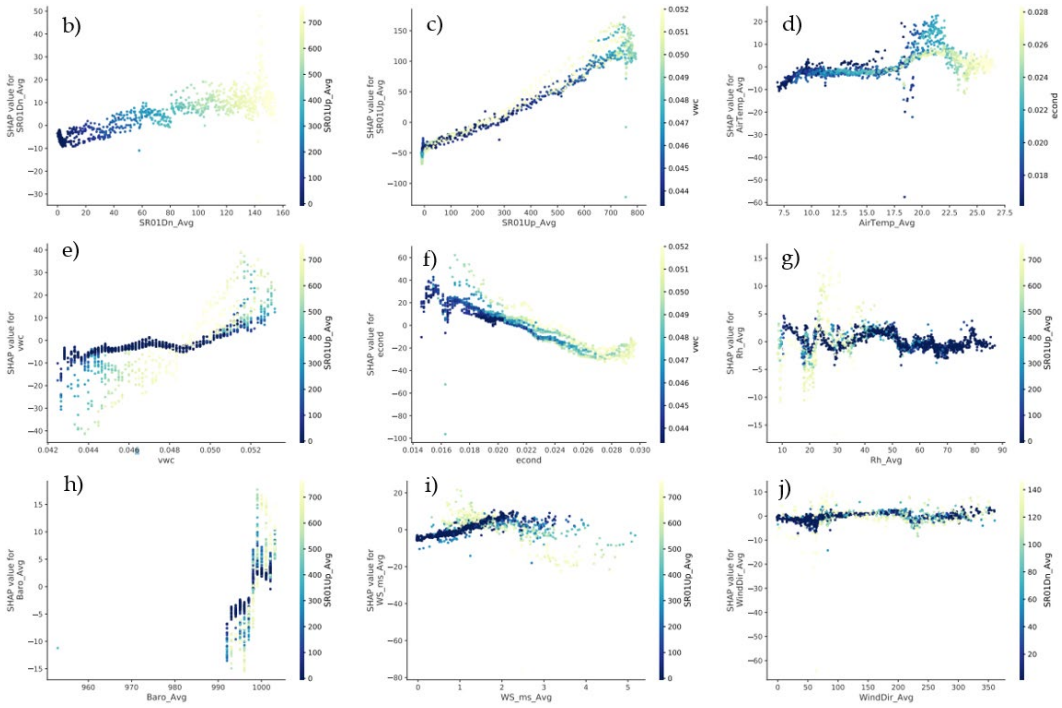

Figure 29 and Figure 30 summarize the environmental effects on ms targets for the CRREL and YPG data set. Similarly, solar radiation is the most important environmental feature for both data sets, with soil moisture second in importance. The next most important feature for the CRREL data set is soil conductivity (with a negative impact), while for YPG, it is air temperature, aligned with the previous study of the md target where the data collection during a warmer air temperature period at CRREL led to an increase in target visibility contrast.

Figure 29. Environmental effects for ms targets using CRREL data.

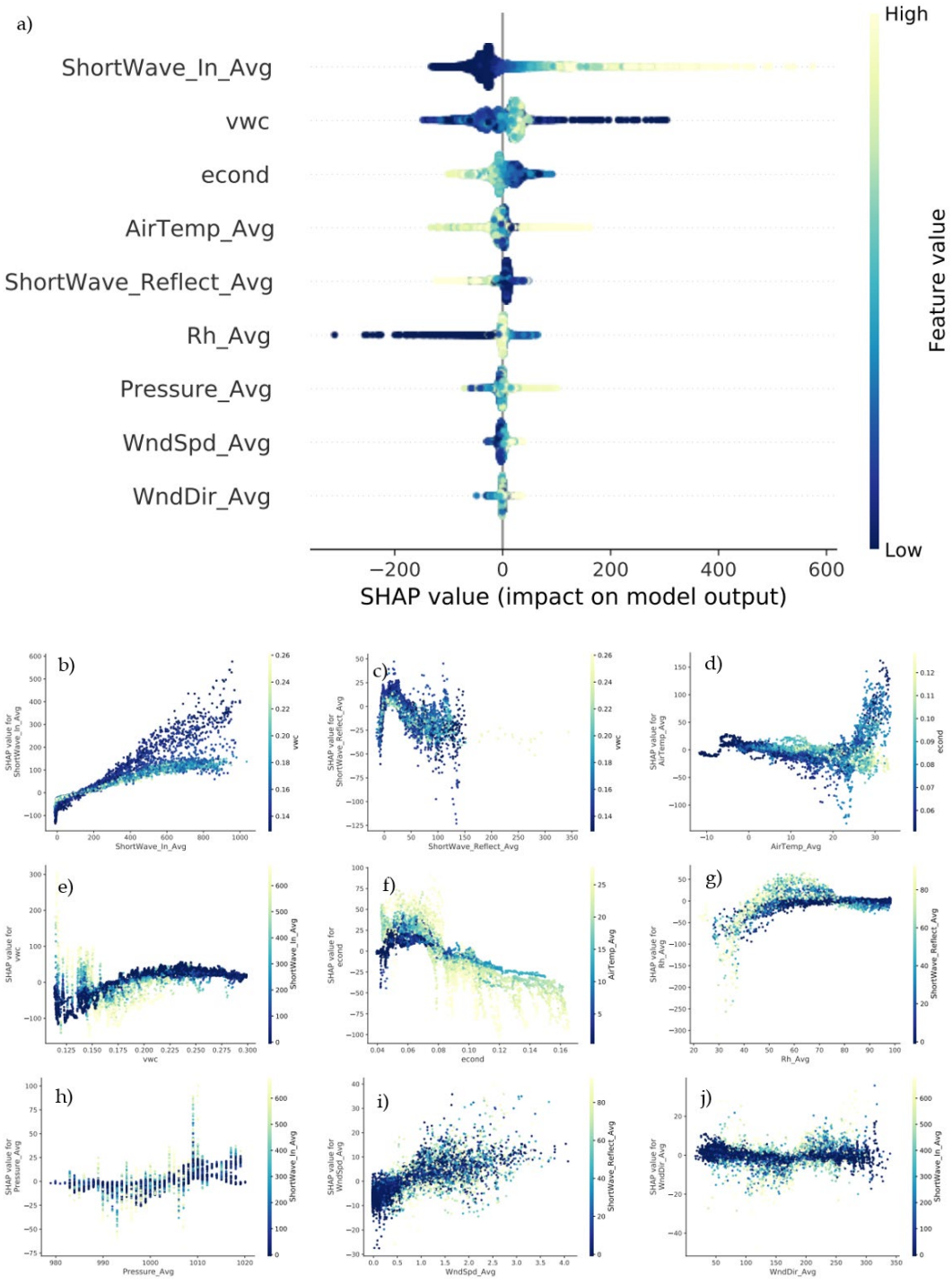

Figure 30. Environmental effects for ms targets using the A310 camera at YPG.

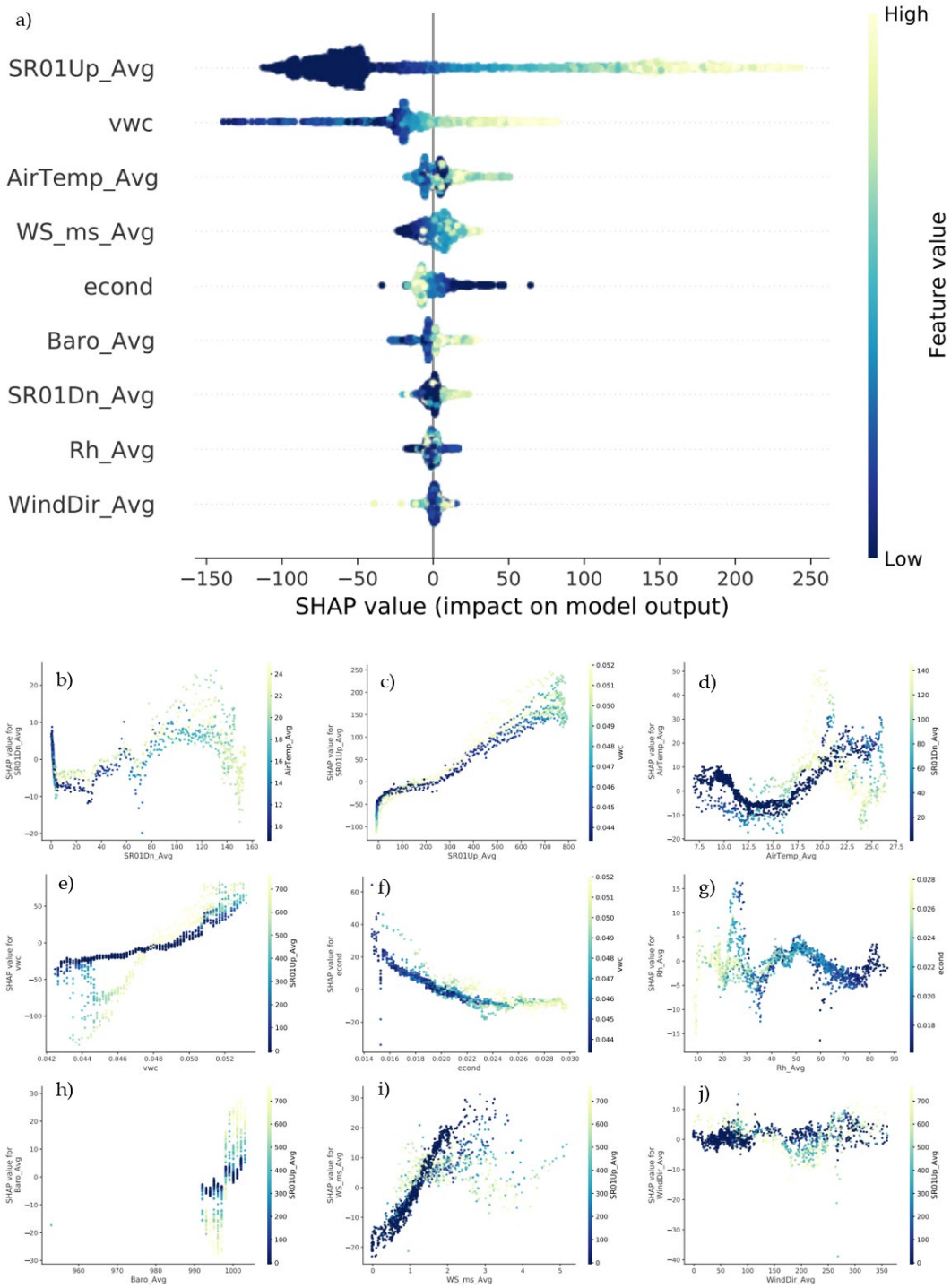

Solar radiation, soil moisture, and air temperature are the three most important environmental features affecting the visibility of Target 52 at YPG (Figure 31). Although Target 52 shares the similar important features as the other targets in terms of size and skin material composition, the

effect of solar radiation and air temperature appears to be reversed when compared to the other targets. The radiance difference between Target 52 and background areas tends to be negatively affected by higher solar radiation, air temperature, and soil moisture. As mentioned previously, Target 52's burial timeline, shape, and innards differ from CRREL's four targets and thus affect the energy flow and radiance.

Finally, scatter plots' interactions were investigated and indicate that increased solar radiation tends to exaggerate trends in the soil conductivity scatter plots. In Figure 31, higher solar radiation levels at lower air temperatures have a greater effect on radiance difference than low air temperatures alone. These results are aligned with earlier outcomes on individual targets. Other interactions between the environmental phenomenology variables and target visibility are apparent in the scatter plots throughout these figures, but since the impact on model output is small, we do not discuss them further.

Figure 31. Environmental effects for Target 52 at YPG using the A310 camera.

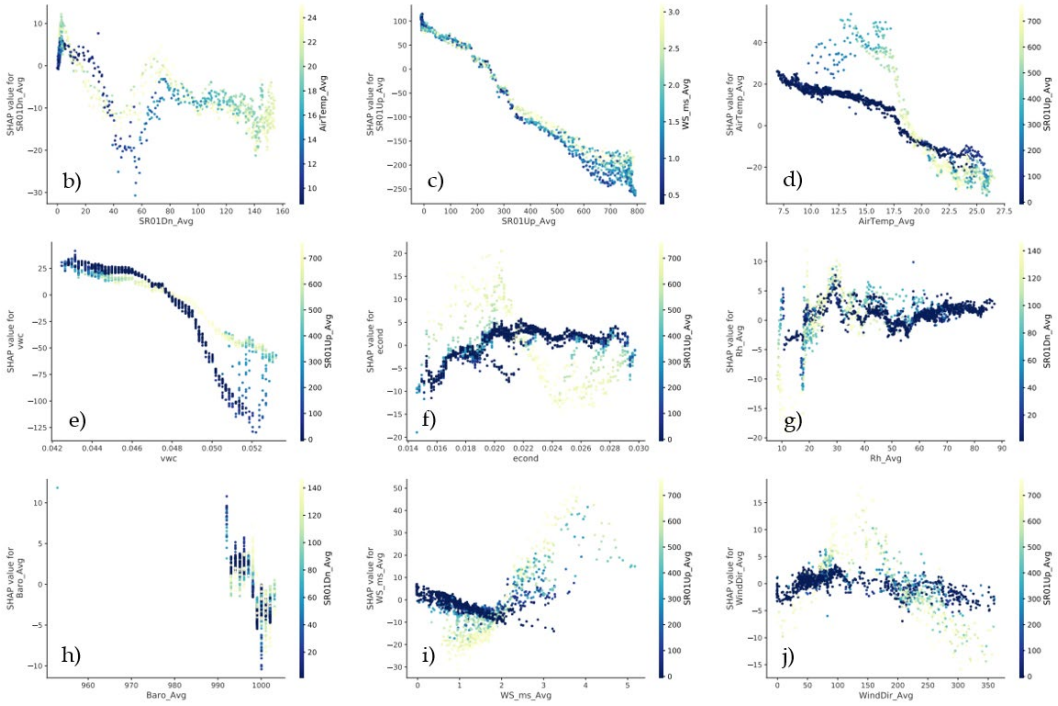

4 Conclusions

The YPG observation data obtained during the 2020 field program brought diversity to the study of buried object detection with the change in geographic location expanding the understanding of environmental effects when combined with the 2018 data collected at CRREL. The change in latitude, biomes, and soil diversity help in identifying the key environmental contributors that were otherwise obscure in the analysis of a single location. This study further validates the suspected phenomena responsible for increased buried target detectability (solar radiation (van De Griend et al. (1985)), as well as those responsible for obscuring results (VWC, Miller et al. (2002)).

The fulcrum of our study centers on the LWIR A310 camera, utilized in both data collection efforts. The A310 camera image observations are similar between the two test sites, with the YPG images exhibiting appreciable soil temperature variability due to soil electrical conductivity, which in turn directly affects VWC accuracy (Figure 15a). Target visibility is largely influenced by incoming solar radiation loading in most cases. However, at times of decreased incoming solar radiation coupled with higher soil moisture levels target visibility can become unpredictable. Periods of low visibility tend to occur with increased soil moisture (Figure 32), but the opposite is also observed (Figure 33) suggesting additional secondary environmental variables play a role under certain conditions. Developing better ways to quantify visibility and to predict the influence of secondary and tertiary environmental effects is an ongoing effort.

Figure 32. Low target visibility examples and associated environmental conditions at the CRREL test plot: (a) incoming solar radiation (W/m2), (b) timestamp and sun angle, (c) soil moisture (%), (d) LWIR image of test plot and camera field of view, (e) Area of Interest radiance difference, and (f) LWIR images of target Areas of Interest.

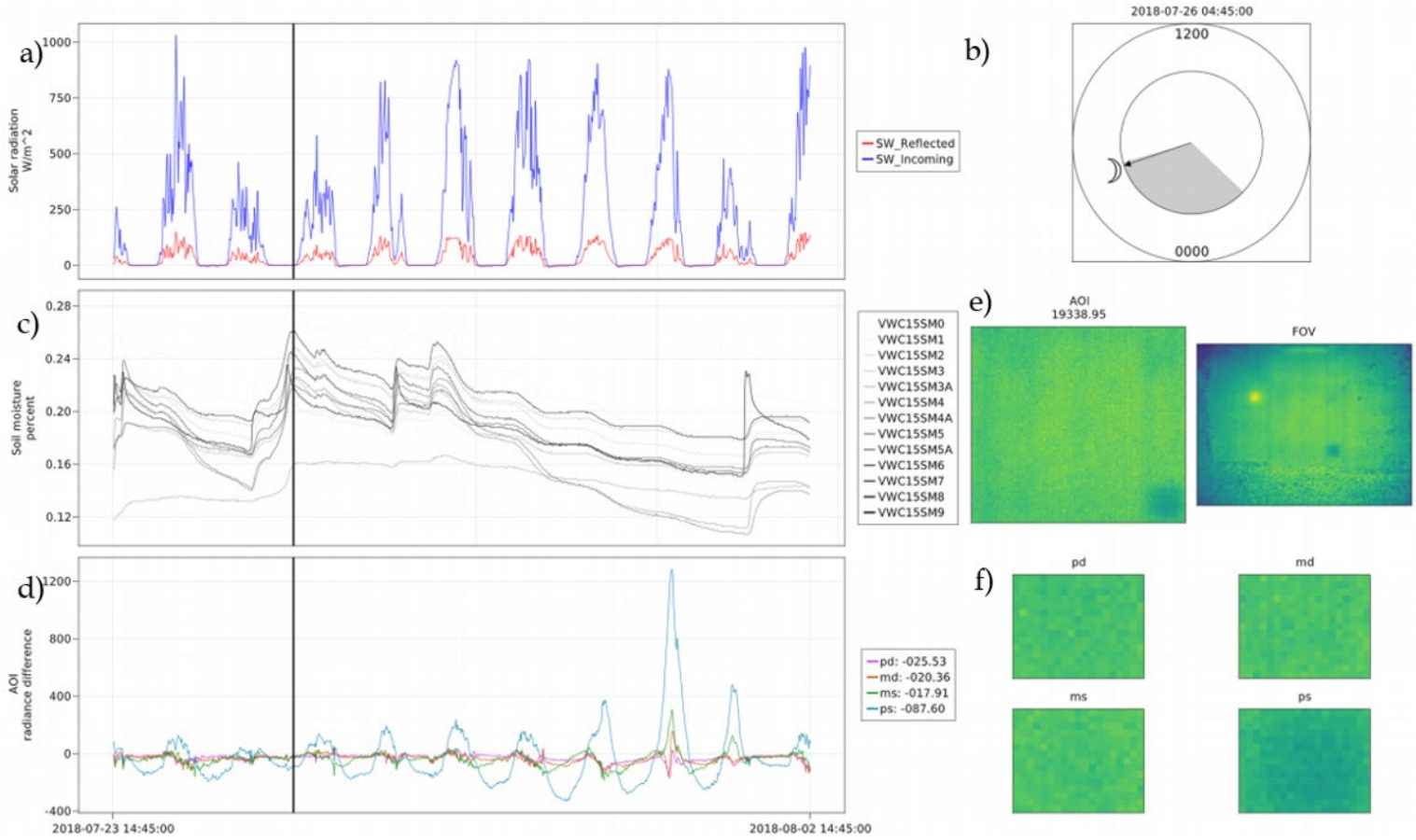

Figure 33. Variation of target visibility and environmental variables prior to target emplacement at the CRREL test plot: (a) incoming solar radiation (W/m2), (b) timestamp and sun angle, (c) soil moisture (%), (d) LWIR image of test plot and camera field of view, (e) Area of Interest radiance difference, and (f) LWIR images of target Areas of Interest.

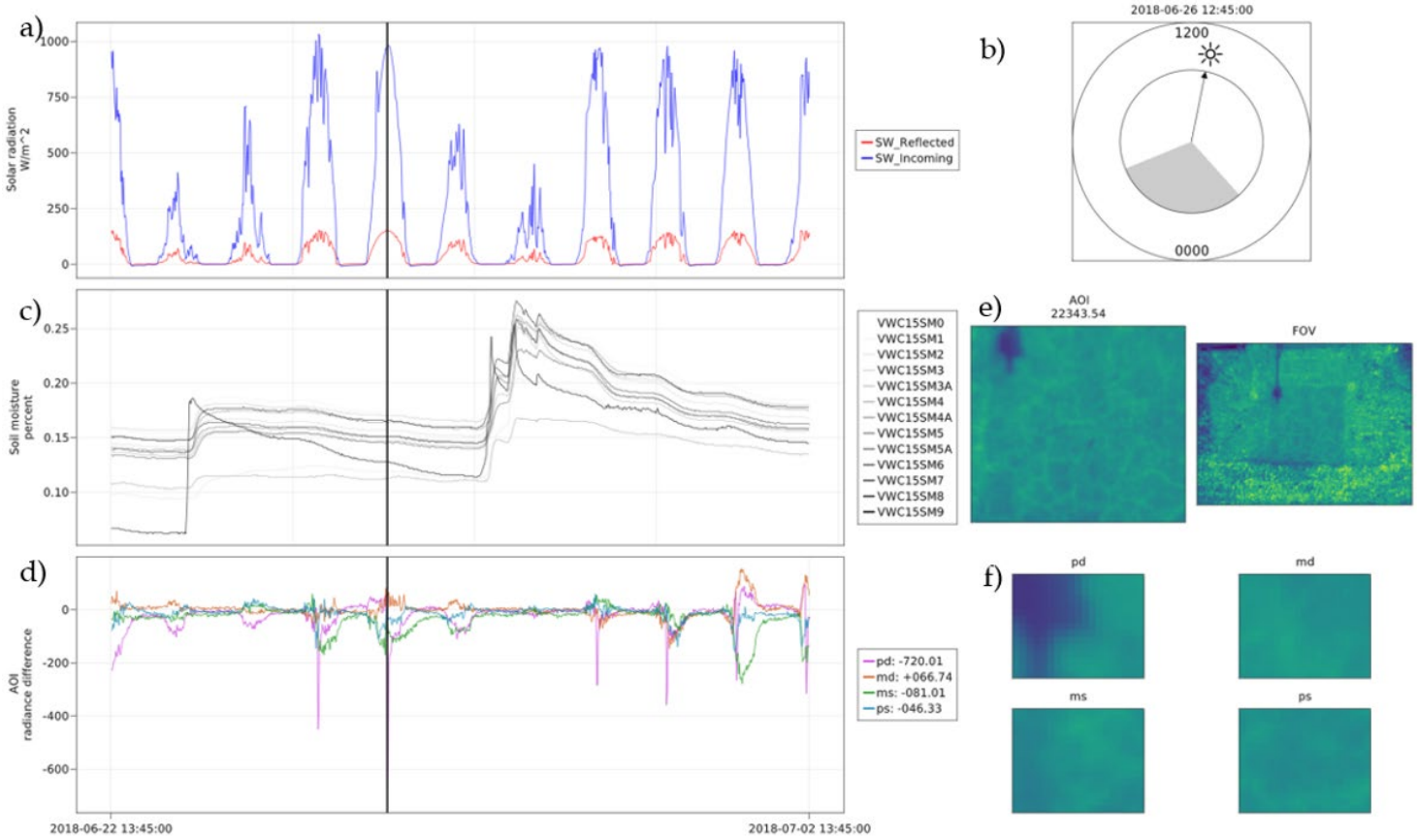

For the MWIR and LWIR cameras, used only at YPG, we find that the MWIR camera performs better in the early evening whereas the LWIR camera performs better in the morning. Target 52, unique to the YPG lane, had contrasting behavior compared to the identical targets located at both test sites. This difference is believed to be due to some combination of the following: (1) period of time between soil disturbance for target emplacement and the study, (2) target filler composition differences, (3) object shape (Target 52 is circular whereas the other targets are rectangular), (4) size (Target 52 surface area is smaller than the other targets), and (5) depth of Target 52 burial (deeper) as compared to the other targets.

The analysis in Section 3.3 revealed that solar loading, soil moisture, air temperature, and soil conductivity are the most important environmental features contributing to target visibility. Increases in solar radiation tend to increase mean radiance differences for all targets except Target 52 at YPG. As soil moisture and conductivity increase, mean radiance differences tend to decrease for all targets but to varying degrees. The analysis also showed that air temperature was more important in the CRREL data set than in the YPG data set. This may be a function of the timing of data collection (late spring to midsummer for CRREL and winter for YPG). Air temperature had an overall positive (nonlinear) trend on model output but in some cases had a somewhat negative trend (e.g., for deep targets at YPG). Wind, humidity, and pressure tend to have little effect on target visibility at both test sites. It remains a question if the study observations are unique to these two sites or have a degree of applicability to other locations at different latitudes, with different soil properties and meteorological conditions, and resulting biomes.

Future work remains to analyze these environmental effects on target visibility more closely. Our focus is on further improving our understanding of more subtle variations in time-lagged environmental phenomenology affects in relation to target visibility. The effect of varying time-dependent secondary environmental phenomenology variables on the predominant primary variables is still yet to be incorporated into the analysis. In addition to an increased understanding of environmental effects on target visibility we are working on incorporating this understanding of environmental phenomological impacts into improving detection performance of automated target recognition software used by the U.S. Army.

References

Chen, T., and C. Guestrin. 2016. "Xgboost: A Scalable Tree Boosting System." *Proceedings of the 22nd ACM SIGKDD International Conference on Knowledge Discovery and Data Mining*, pp. 785–94.

Clausen, J. L., S. Frankenstein, J. R. Dorvee, A. Workman, B. F. Morriss, K. J. Claffey, T. M. Sobecki, et al. 2021. *Spatial and Temporal Variance of Soil and Meteorological Properties Affecting Sensor Performance—Phase II*. ERDC/CRREL TR-21-10. Hanover, NH: U.S. Army Corps of Engineers, Engineer Research and Development Center, Cold Regions Research and Engineering Laboratory.

Clausen, J. L., J. R. Dorvee, A. Wagner, S. Frankenstein, B. F. Morriss, K. J. Claffey, T. M. Sobeck., et al. 2020. *Spatial/Temporal Variance in the Thermal Response of Buried Objects*. ERDC/CRREL TR-20-10. Hanover, NH: U.S. Army Corps of Engineers, Engineer Research and Development Center, Cold Regions Research and Engineering Laboratory.

Crews, J. B., D. J. Page, S. C. Rybarski, E. J. Hartshorn, W. B. Weir, D. E. Sabol, B. F. Lyles, J. M. Healey, M. B. Hausner, and E. V. McDonald. 2019. *Enhanced Soil Electromagnetic Parameter Acquisition Using the Open Hull Dual Aperture Measurement Network (OHDAMN)*, 58 pp. Report prepared for USACE ERDC-CRREL. Reno, NV: Desert Research Institute.

Davis, J. L., and A. P. Annan. 2002. "Ground Penetrating Radar to Measure Soil Water Content." In J. H. Dane and G. C. Topp (eds.), *Methods of Soil Analysis: Part 4—Physical Methods*. Madison, WI: Soil Science Society of America, 446–63.

Hausner M. B., E. V. McDonald, J. B. Crews, E. J. Hartshorn, K. L. Minatre, D. J. Page, S. C. Rybarski, D. E. Sabol, B. Sion, and W. B. Weir. 2019. *Intra-Site Soil Variability on the Yuma Proving Ground Countermine Site*. Report prepared for the U.S. Army Yuma Proving Ground. Reno, NV: Desert Research Institute.

Hausner, M. B. W. B. Weir, and E. McDonald. 2020. *Exploratory Numerical Modeling of Heat and Mass Transfer around Buried Munitions*. Report prepared for USACE ERDC-CRREL. Reno, NV: Desert Research Institute.

Howington, S. E., J. R. Ballard Jr., N. V. Kala, A. C. Trautz, M. D. Bray, M. W. Farthing, and A. M. Hines. 2019. "Exploitable Synthetic Sensor Imagery from High-Fidelity, Physics-Based Target and Background Modeling." Proc. SPIE 11158, Target and Background Signatures V, 1115809. https://doi.org/10.1117/12.2532923.

Khanafer, K., and K. Vafai. 2002. "Thermal Analysis of Buried Land Mines over a Diurnal Cycle." *IEEE Transactions on Geoscience and Remote Sensing* 40 (2):461–73.

Lundberg, S. M., G. Erion, H. Chen, A. DeGrave, J. M. Prutkin, B. Nair, R. Katz, J. Himmelfarb, N. Bansal, and S. Lee. 2020. "From Local Explanations to Global Understanding with Explainable AI for Trees." *Nature Machine Intelligence* 2 (1): 2522–5839.

Lundberg, S. M., and S. Lee. 2017. "A Unified Approach to Interpreting Model Predictions." In I. Guyon, U. V. Luxburg, S. Bengio, H. Wallach, R. Fergus, S. Vishwanathan, and R. Garnett (eds.), *Advances in Neural Information Processing Systems* 30: 4765–74. Red Hook, NY: Curran Associates, Inc.

Lundberg, S. M., B. Nair, M. S. Vavilala, M. Horibe, M. J. Eisses, T. Adams, D. E. Liston, et al. 2018. "Explainable Machine-Learning Predictions for the Prevention of Hypoxaemia during Surgery." *Nature Biomedical Engineering* 2 (10): 749–60.

Mattikalli, N. M., E. T. Engman, L. R. Ahuja, and T. J. Jackson. 1998. "Microwave Remote Sensing of Soil Moisture for Estimation of Profile Soil Property." International Journal of Remote Sensing 19(9): 1751–67.

Miller T., B. Borchers, J. M. H. Hendrickx, S. Hong, H. A. Lensen, P. B. W. Schwering, and J. Rhebergen. 2002. "Effect of Soil Moisture on Landmine Detection Using Ground Penetration Radar." *Proceedings of SPIE 4742, Detection and Remediation Technologies for Mines and Minelike Targets VII*. https://doi.org/10.1117/12.479099.

Pan, H. L., and L. Mahrt. 1987. "Interaction between Soil Hydrology and Boundary-Layer Development." *Boundary-Layer Meteorology* 38(1–2): 185–202.

Retief, P., C. J. Willers, and M. S. Wheeler. 2003. "Prediction of Thermal Crossover Based on Imaging Measurements over the Diurnal Cycle, Geo-Spatial and Temporal Image and Data Exploitation III." *International Society for Optics and Photonics* 5097: 58–69.

Sharma, G., W. Wu, and E. N. Dalal. 2005. "The CIEDE2000 Color-Difference Formula: Implementation Notes, Supplementary Test Data, and Mathematical Observations, Color Research and Application: Endorsed by Inter-Society Color Council, The Colour Group (Great Britain), Canadian Society for Color, Color Science Association of Japan, Dutch Society for the Study of Color, The Swedish Colour Centre Foundation, Colour Society of Australia." *Centre Français de la Couleur* 30(1): 21–30.

Štrumbelj, E., and I. Kononenko. 2014. "Explaining Prediction Models and Individual Predictions with Feature Contributions." *Knowledge and Information Systems* 41 (3):647–65.

van De Griend, A. A., P. J. Camillo, and R. J. Gurney. 1985. "Discrimination of Soil Physical Parameters, Thermal Inertia, and Soil Moisture from Diurnal Surface Temperature Fluctuations." *Water Resources Research* 21 (7): 997–1009.

Appendix A

A.1. CS655 soil moisture probe location. The labels correspond to variable names in the data.

Table A-1. CS655 soil moisture probe location.

Label	Location	Depth (cm)
31837	10 cm south of box #4	40
31838	10 cm south of box #4	20
31839	10 cm south of box #4	5
31840	7 cm west of box #1	5
31842	50 cm west of box #1	5
40332	west edge of box #4	5

A.2. Temperature thermistor location. The labels correspond to variable names in the data.

Table A-2. Temperature thermistor location.

Label	Location	Depth (cm)
1	under box #1	
2	west side of box #1	10
3	top of box #1	
4	under box #2	
5	west of box #2	
6	top of box #2	
7	top of puck #1	
8	top of puck #2	
9	under puck #2	
10	on surface between puck #2 and box #2	
11	under box #3	
12	west of box #3	
13	top of box #3	
14	under box #4	
15	west side of box #4	

Label	Location	Depth (cm)
16	top of box #4	
17	under puck #3	
18	top of puck #3	
19	top of puck #4	
20	on surface between puck #3 and box #4	

REPORT DOCUMENTATION PAGE

Form Approved
OMB No. 0704-0188

1. REPORT DATE *(DD-MM-YYYY)*	2. REPORT TYPE	3. DATES COVERED *(From - To)*
08-2022	Final	

4. TITLE AND SUBTITLE

Thermal Infrared Comparison Study of Buried Objects between Humid and Desert Test Beds

5a. CONTRACT NUMBER

5b. GRANT NUMBER

5c. PROGRAM ELEMENT NUMBER
0602712A

6. AUTHOR(S)

M. Musty, V. Truong, J. L. Clausen, S. Frankenstein, C. Williams, A. Trautz, S. Howington, and R. Kala

5d. PROJECT NUMBER
468349

5e. TASK NUMBER
A1010

5f. WORK UNIT NUMBER

7. PERFORMING ORGANIZATION NAME(S) AND ADDRESS(ES)

U.S. Army Engineer Research and Development Center
Cold Regions Research and Engineering Laboratory
72 Lyme Road
Hanover, NH 03755-1290

8. PERFORMING ORGANIZATION REPORT NUMBER

ERDC/CRREL-TR-22-10

9. SPONSORING / MONITORING AGENCY NAME(S) AND ADDRESS(ES)

Night Vision and Electronic Sensors Directorate (NVESD)
AMSEL-RD-NV-RM-OPS
10221 Burbeck Road
Ft. Belvoir, VA 22060-5806

10. SPONSOR/MONITOR'S ACRONYM(S)

11. SPONSOR/MONITOR'S REPORT NUMBER(S)

12. DISTRIBUTION / AVAILABILITY STATEMENT
Approved for public release; distribution is unlimited.

13. SUPPLEMENTARY NOTES

14. ABSTRACT

This study pertains to the thermal variations caused by buried objects and their ramifications on soil phenomenology. A multitude of environmental conditions were investigated to observe the effect on thermal infrared sensor performance and detection capabilities. Correlations between these external variables and sensor contrast metrics enable determinable key factors responsible for sensor degradation. This document consists of two parts. The first part is a summary of data collected by the U.S. Army Corps of Engineers, Engineer and Research and Development Center Cold Regions Research and Engineering Laboratory (ERDC-CRREL), ERDC-Geotechnical Structures Laboratory, and Desert Research Institute at the Yuma Proving Ground (YPG) site in February 2020 and observations from this activity. The second part is a comparison of target visibility between data collected at YPG and data collected at the ERDC-CRREL test site in 2018.

15. SUBJECT TERMS
Military surveillance; Detectors; Infrared detectors; Environmental conditions; Soils--Thermal properties; Earth temperature

16. SECURITY CLASSIFICATION OF:			17. LIMITATION OF ABSTRACT	18. NUMBER OF PAGES	19a. NAME OF RESPONSIBLE PERSON
a. REPORT	b. ABSTRACT	c. THIS PAGE			19b. TELEPHONE NUMBER *(include area code)*
Unclassified	Unclassified	Unclassified	None	66	